Skeletal quartz and dendritic biotite: Witnesses of primary disequilibrium growth textures in an alkali-feldspar granite

Pierre Barbey, François Faure, Jean-Louis Paquette, Karine Pistre, Cyrille Delangle, Jean-Paul Gremilliet

Skeletal quartz and dendritic biotite: witnesses of primary disequilibrium growth textures in an alkali-feldspar granite

Pierre Barbey[1*], François Faure[1], Jean-Louis Paquette[2], Karine Pistre[3], Cyrille Delangle[4], Jean-Paul Gremilliet[4]

[1] *Université de Lorraine, CNRS, CRPG, F-54000 Nancy, France*
[2] *Université Clermont Auvergne, CNRS, IRD, OPGC, Laboratoire Magmas et Volcans, F-63000 Clermont-Ferrand, France*
[3] *Université de Lorraine, CNRS, GeoRessources, F-54000 Nancy, France*
[4] *Centre Terrae Genesis, F-88120 Le Syndicat, France*

* Corresponding author:
E-mail: pierre.barbey@univ-lorraine.fr

Highlights

- Cathodoluminescence imaging reveals the presence of two generation of quartz
- The first generation corresponds to both rounded and skeletal grains
- The second generation (overgrowths) led to partly equilibrated texture
- Biotite shows variable morphology, including skeletal and dendritic habits
- These textures are interpreted to result from primary disequilibrium growth

Abstract

We describe a case of S-type alkali-feldspar granite (quartz/K-feldspar/plagioclase/ biotite/garnet ~ 30/35/20/13/2 vol. %) showing skeletal and dendritic textures. It consists of three nested units distinguishable by the size of biotite crystals: a first-emplaced unit characterized by small biotite flakes (0.4–9 mm); a second unit with cm-sized biotite platelets (0.3–28 mm) outlining a syn-magmatic foliation; and a third unit formed of large biotite plates (0.7–850 mm) showing dendritic and radial growth patterns.

Quartz occurs mostly as rounded to euhedral grains, but also shows complex shapes (serrated outline, re-entrants, etc.). Cathodoluminescence imaging reveals that grains consist of both rounded and skeletal bluish cores (quartz-1) rimmed by reddish overgrowths (quartz-2) that lead locally to the coalescence of neighbouring grains and equilibrated texture. Biotite is poikilitic enclosing dominantly quartz grains but also in lesser amount plagioclase and garnet. In the third unit, biotite shows textures typical of dendritic growth (bifurcating, radiating or branching structures, skeletal core). Plagioclase ($An_{\leq 25}$) occurs as small euhedral to subhedral grains scattered in the matrix or forming glomerophyric aggregates. K-feldspar ($Or_{74–100}$) mostly forms an almost equilibrated mosaic of anhedral perthitic crystals; it also appears in association with albite as a secondary phase replacing plagioclase. The crystallization sequence started with garnet, then proceeded with quartz, plagioclase, biotite and K-feldspar, ended with cordierite, and was followed by subsolidus reequilibration.

The variability in size and morphology of quartz and biotite is interpreted in terms of variable undercooling depending on temperature of the host-rocks and on more or less intense degassing of magma batches with variable melt water content. Here, rapid crystallization prevented significant textural reequilibration and allowed the initial crystallization textures of quartz to be preserved. Overall, this study shows that behind the common “coarse-grained” texture of quartz in granite, subsist primary disequilibrium crystallization textures.

Keyword: texture; dendritic growth; granite; undercooling

1. Introduction

During their thermal evolution, igneous rocks tend to approach textural equilibrium to minimize excess surface energy. This is more particularly visible in plutonic rocks owing to mass redistribution within the crystal pile (e.g. Lesher and Walker, 1988), which leads to textural coarsening (e.g. Higgins, 2011), a process well illustrated by the mafic layered igneous complexes (e.g. Cawthorn, 1996). Even though the thermal history and related textural maturity can, to some extent, be deciphered from the study of dihedral angles (Holness, 2005; Holness et al., 2007a, 2007b, 2007c) or crystal size distribution (Cashman and Marsh, 1988; Higgins, 2011; Magee et al., 2010; Marsh, 1988), studies of igneous rocks are often facing with the issue to know to what extent the textures we observe are representative of the initial stages of crystallization.

Experimental works led to a better understanding of crystal morphology in relation with the dynamics of magma crystallization in rapidly cooled rocks (e.g. Lofgren, 1980). For instance, shapes of plagioclase in basalts or of olivine in spinifex-textured komatiites, first attributed to quenching, was shown to be related to cooling rates (Donaldson, 1976, 1982; Lofgren, 1974; Lofgren & Donaldson, 1975). Later, Faure et al. (2003, 2006) determined experimentally the respective role of undercooling, cooling rate and thermal gradient on the shape and orientation of olivine crystals. Phosphorus zoning patterns in olivine from diverse volcanic rocks and meteorites have also revealed that olivine phenocrysts are cored by dendrites (Libourel et al., 2018; Milman-Barris et al., 2008; Welsch et al., 2013, 2014), a characteristic attributed to primary variations in crystal growth rate (Milman-Barris et al., 2008). This observation has been extended to olivine from Mid-Atlantic Ridge gabbro and from mafic-ultramafic intrusions (Welsch et al., 2014; Xing et al., 2017). This led Welsch and co-workers to conclude that diffusion-controlled crystal growth is an important feature of primary textures in igneous rocks. Others authors also emphasized that high supersaturation

92 and high growth rate are not uniquely driven by rapid cooling, but could also be enhanced by
93 shift in the liquidus temperatures related to change in melt water content (Donaldson, 1974;
94 Vernon, 1985; Almeev et al., 2007; Médard and Grove, 2008).
95 Concerning silicic plutonic rocks, crystallization experiments show that quartz exhibits
96 different morphologies as a function of the degree of undercooling (MacLellan and Trembath,
97 1991; Swanson and Fenn, 1986). At small ΔT, quartz develops subhedral to euhedral shapes
98 by interface-controlled growth mechanisms; whereas at larger ΔT, diffusion-controlled
99 growth mechanisms promote the formation of skeletal shapes in relation with compositional
100 gradient at the melt-crystal interface. Under longer experimental runs, skeletal quartz
101 becomes rounded by the reduction in the degree of faceting and the partial infilling of skeletal
102 crystals. Besides, preservation of primary compositional growth patterns in quartz has been
103 found in dacites and rhyolites (Ackerson et al., 2018; Ahmed, 2011; Götze et al., 2001; Seitz
104 et al., 2016; Watt et al., 1997); and disequilibrium growth textures (skeletal and dendritic) are
105 also known in some specific silicic plutonic rocks, such as pegmatites (e.g. Frindt and
106 Haapala, 2004; Haapala and Lukkari, 2005; Ivanov and Grozdanov, 2001; London, 2009;
107 Müller et al., 2002; Shannon et al., 1982; Swanson and Fenn, 1986) and orbicular granites
108 (e.g. Decitre et al., 2002; Smillie and Turnbull, 2014).
109 Overall, it can be expected that the common “coarse-grained” texture of granite might
110 conceal primary disequilibrium crystallization textures partly hidden (if not erased) by the
111 subsequent thermal evolution. The aim of this study is to address this issue from an
112 interesting case of alkali-feldspar granite. After description of phase assemblages and
113 chemical compositions, we focus on the characterization of textures to demonstrate that this
114 granite preserves primary disequilibrium growth textures recorded in the morphology of
115 quartz and biotite.
116

2. Samples

The granite studied here is located in the Central Vosges domain, eastern France (Fluck et al., 1991; Skrzypek et al., 2014). The outcrop, ca. 250 m long, is located along the road D42, 2 km to the NW of Eloyes (48°06'21.50" N – 06°35'30.50" E). A cross-section (Fig. 1) shows that the alkali-feldspar granite body forms the most part of the road cut, being bounded (faulted contacts) to the NW by intrusive coarse-grained porphyritic granite (Remiremont granite belonging to the Central Vosges granite association; Tabaud et al., 2015), and to the SW by migmatitic biotite gneisses (metatexites to diatexites). Therefore, its exact extension and geometry, seemingly a dike, remain unknown. A presentation of its geological context and emplacement age is given in Supplementary material SM.1.

The granite corresponds to a pale pink rock, consisting of a fine- to medium-grained quartzofeldspathic matrix with limited amounts of ferromagnesian minerals. Considering the matrix grain size (average of ca. 0.25 mm), the rock appears to be at the limit between granite and microgranite according to the grain size classification of Gillespie & Styles (1999). The matrix consists of quartz (30–40 vol.%), K-feldspar (30–40 vol. %) and plagioclase (20–25 vol. %), whereas the ferromagnesian mineral phases consist of garnet (≤ 7 vol. %), biotite (5–15 vol. %) and scarce late-magmatic cordierite (± tourmaline). Accessory minerals are zircon, monazite, ilmenite and Ti-oxide. Secondary phases are muscovite, albite and K-feldspar replacing primary feldspars; green biotite, chlorite, and hematite replacing garnet; and chlorite and prehnite replacing biotite. The variable size of biotite led us to distinguish three magmatic units (Fig. 1):

- *Unit-1* forms the external parts of the igneous body. It contains medium-grained, randomly distributed, biotite flakes outlining a faint syn-magmatic fabric (Fig. 2a, b). The grain size of the matrix lies mostly between 0.3 and 0.6 mm, though ranging from 0.05 mm to 1.7 mm for the largest K-feldspar crystals (Fig. 2c).

- *Unit-2* forms the core of the body. Biotite is mostly medium- to coarse-grained and outlines a widespread syn-magmatic foliation (Fig. 3a-c), trending ENE-WSW, steeply dipping (ca. 80°) and locally accompanied with a weak lineation. The grain size of the matrix lies between 0.3 and 0.8 mm (Fig. 3d). Small mafic and autolithic enclaves (6–8 cm in diameter), wrapped up by the foliation, are observed locally (Fig. 3c).

- *Unit-3* corresponds chiefly to a ca. 2-metre-thick dyke-like body, but also to scarce small veins within Unit-2. It is characterized by the presence of large biotite crystals showing a specific textural organization (Fig. 4a-c) described farther. The grain size of the matrix lies mostly between 0.2 and 0.6 mm (Fig. 4d), though some K-feldspar crystals may reach 1.5 cm in length. A faint foliation occurs locally in connection with small shear-zones.

Internal contacts between the three units are sharp with no chilled margin and no crystals nucleation on the contacts; they are marked mainly by change in the biotite size and locally by loss of the fabric (between Unit-2 and Unit-3). Textures and mineral compositions are presented in more detail in section 4.

3. Whole-rock compositions

Whole-rock major and trace element compositions are given in Table 1 and analytical conditions in the Supplementary material SM.2. The rock is granitic ($69.7 < SiO_2 < 75.2$ wt. %), with a normative composition classifying it as alkali-feldspar granite (Q' = 34.9–42.4; ANOR = 0.5–5.4) according to Streckeisen and Le Maitre (1979). It is peraluminous ($[Al_2O_3]/[CaO+Na_2O+K_2O] = 1.22–1.38$), with Mg# values ranging from 33 to 41 (total iron as Fe^{2+}), plotting close to the ferroan line in the classification diagram of Frost et al. (2001) (not shown). Trace element contents are low, with the notable exception of Ba, Rb and Zr (331–689, 211–264 and 72–149 ppm, respectively). Trace element discriminant ratios (Whalen et al., 1987) corroborate its S-type chemistry (Zr+Nb+Ce+Y = 139–246 ppm;

10^4*Ga/Al = 2.1–2.4), corresponding to low-Ca unfractionated granite (X_{Sr} < 0.15 and X_{Rb} < 0.35) according to the nomenclature of El Bouseily and El Sokkary (1975). Zircon saturation thermometry (Watson and Harrison, 1983) yields temperatures in the range 740–800° C. Sr and Nd isotopic compositions (Table 2) show $^{87}Sr/^{86}Sr_{(330\ Ma)}$ initial ratio of 0.726, $\varepsilon Nd_{(330\ Ma)}$ value of -8.2, and Nd model age (T_{DM}) of 1865 Ma consistent with zircon U–Pb data attesting to the presence of inherited core at 1.9 Ga (see Supplementary material SM.1).

Multi-element plot normalized to Primitive Mantle (Fig. 5a) shows depletion in Ba, U, Th, Ta, Nb, Sr, Eu and Ti. K/Rb (198–254) and Y/Ho (27–29) ratios are similar to values of common igneous rocks, and the Zr/Hf ratio (33–37) is close to that of most terrestrial rocks (~38). Nb/Ta ratio (7–14, with the exception of Unit-1 with values at 19 and 23) compared to Zr/Hf ratio corresponds to that of barren granites (Ballouard et al., 2016). However, the K/Ba (73–194), La/Nb (1.7–5.3) and La/Ta (19–123) ratios are significantly higher than those of common magmatic rocks, suggesting non-CHARAC behaviour of Ba, Nb and Ta, and thus, the possible effect of hydrothermal fluids (e.g. Bau, 1996; Jahn et al., 2001). Rare earth elements (REE) normalized to chondrite (Fig. 5b) show moderately fractionated light REE ($[La/Sm]_N$ = 2.9–5.2), negative Eu anomalies (Eu/Eu* = 0.3–0.7) and weakly fractionated heavy REE ($[Gd/Yb]_N$ = 0.6–0.8). The negative slope and concave-downward shape of heavy REE, along with t_3 parameter ($[Tb/Tb^* \times Dy/Dy^*]^{0.5}$; Irber, 1999) around 1.01–1.13, could suggest a possible weak tetrad effect. Nevertheless, the $TE_{1,3}$ parameter ($[t_1 \times t_3]^{0.5}$, with t_1 = ($[Ce/Ce^* \times Pr/Pr^*]^{0.5}$; Irber, 1999) remains low (1.00–1.09) compared to the minimum value (1.1) generally considered to be significant of the tetrad effect (Irber, 1999).

4. Textures and mineral compositions

4.1. Quartz

In optical microscopy quartz appears mostly as euhedral (sub-hexagonal or quadrangular) to subhedral (rounded) grains. Nevertheless, more complex shapes are observed: (i) grains showing serrated outline resembling incipient branching arms (Fig. 6a); (ii) crystals with equilibrated grain boundaries (Fig. 6b); (iii) triangular extensions and thin films (in optical continuity with a main quartz grain) pervading feldspar-feldspar or feldspar-biotite grain boundaries (Fig. 6c, d); (iv) crystals with rounded re-entrants (Fig. 6e) as commonly observed in high-cooling magmas (rhyolite); and (v) anhedral grains in interstitial position probably pseudomorphing the residual melt-filled porosity (Fig. 6f).

Cathodoluminescence imaging reveals that quartz grains have an internal structure consisting of a bluish core commonly surrounded by reddish overgrowth. The cores correspond to more or less rounded to elliptical grains with regular to wavy outlines (Fig. 7a), or to skeletal grains with jagged outlines (Fig. 7b), branching structures (Fig. 7c) and hollow cores (Fig. 7a, d). Overgrowths are not systematically present and do not always form a continuous rim all around cores (e.g. Fig. 7a, b); they commonly lead to the coalescence of neighbouring grains, giving rise locally to equilibrated granoblastic texture (Fig. 7e). Textural relationships between quartz and biotite show unambiguously that cores predate biotite crystallization, whereas overgrowths formed synchronously with biotite. This is indicated by (i) blue cores directly in contact with biotite without overgrowth; (ii) space between two blue cores filled with quartz-2 and biotite; (iii) thin red quartz outgrowths along the cleavage of biotite; and (iv) reddish quartz forming symplectitic intergrowths with biotite, for some of them in continuity with the overgrowth surrounding bluish quartz grains (Fig. 7f).

Quartz grain size varies from one unit to another. Sizes were measured in thin section considering the long axes of the whole grains, even though this undoubtedly introduces a bias due the presence of overgrowths. Nevertheless, the small thickness of these overgrowths, their non-systematic occurrence and their similarity in all units lead us to consider that the size

variation of all grains is controlled by the size variation of cores. In Unit-1, quartz grain size ranges from 0.04 to 0.6 mm with a median at 0.14 mm (Fig. 8a). In Unit-3, a similar range (0.05 to 0.6 mm) is observed, but the sizes appear a little more homogeneous with ca. 57 % of the grains between 0.15 and 0.25 mm (Fig. 8b, c). In Unit-2, quartz population shows higher dispersion, with sizes ranging from 0.05 to 1.3 mm and medians ≥ 0.24 mm (Fig. 8d–f). On the whole, although the average grain size does not significantly differ from one unit to the other, we note that the histograms of size distribution differ in each unit, the standard deviation is higher in the Unit-2 attesting to its greater heterogeneity, and the proportion of grains with a size higher than 0.25 mm markedly increases from Unit-1 (ca. 15 %) to Unit-3 (ca. 25 %) and Unit-2 (30–55 %).

4.2. Garnet

Garnet occurs as euhedral to subhedral rounded grains (Fig. 9a, b), with size ranging between 0.4 and 2.0 mm. It may occur as inclusion in feldspar or in biotite (in this case, it may show partial retrogression; Fig. 9c). Garnet corresponds dominantly to a binary solid solution of almandine (77.6 ± 3.6 mol. % on average) and pyrope (15.7 ± 3.8 %), with limited amounts of spessartite (4.3 ± 2.0 %) and grossularite (2.4 ± 0.4 %). It is slightly more Mg-rich in the Unit-3 compared to the other units (Fig. 10a), whereas garnet from Unit-1 has a slightly lower content of spessartite + grossularite.

4.3. Biotite

The common feature of biotite in all units is to be poikilitic (Fig. 11a), enclosing dominantly quartz grains but also in much smaller amount plagioclase and garnet. In Unit-1, biotite occurs as small rounded flakes to slightly larger anisometric crystals (Fig. 2a, b) with rather homogeneous sizes, mostly ≤ 5 mm (range 0.4–9 mm, Fig. 12a). In Unit-2, biotite occurs as

241 larger platelets parallel or at high angle to the fabric (Fig. 3d). It is more heterogeneous in size
242 (Fig. 3a), with length ranging from 0.3 to 28 mm (Fig. 12b); this heterogeneity being
243 enhanced by the presence of zones showing higher grain size (Fig. 3c). Some of the largest
244 crystals display branching bifid structure and hollow cores (Fig. 11b and 11e, respectively). In
245 Unit-3, biotite forms a network of large plates arranged at high angle to each other (Fig. 4b,
246 c), with sizes ranging from 0.7 to 850 mm (Fig. 12c). Its shape encompasses rounded or
247 slightly anisometric millimetre-sized flakes similar to those of the former units, to large
248 blades with width/length ratio around 0.4 (Fig. 4a). Radial growth patterns (Fig. 4b, c) and
249 dendritic shapes (Fig. 11c, d) are characteristic of biotite in this unit. It also shows hollow
250 cores filled with feldspathic material between thin biotite platelets in crystallographic
251 continuity with the main crystal (Fig. 11f). There is a clear difference in the histograms of
252 biotite size distribution between the three units: in Unit-1 the distribution is tightened around
253 1.4 mm, while in Unit-2 it is more heterogeneous with an average around 4.2 mm; histogram
254 of Unit-3 is given only for information, as it has very little significance due to the branching
255 nature and stronger anisotropic shape of the biotite plates.
256 Biotite is slightly magnesian (Fig. 10b), with X_{Mg} ratios ranging from 0.30 to 0.49 (0.41 ±
257 0.04 on average); TiO_2 contents are mostly around 3.1 % (range 1.07–4.42 wt. %); and Al^{VI}
258 contents range from 0.54 to 1.60 atoms per formula unit (apfu). Its high total Al content (Al_{tot}
259 = 3.1–4.4 apfu) with respect to Mg (1.2–2.2 apfu) is consistent with the peraluminous
260 character of the host-rock. Secondary green biotite crystals, mainly developed at the expense
261 of garnet, depart from this compositional field, with higher Al^{VI} values (0.9–1.6 compared to
262 ≤ 0.9) and lower TiO_2 contents (mostly ≤ 1.0 wt. % compared to 3.1 % on average).
263
264 *4.4. Cordierite and tourmaline*

265 Cordierite occurs as scarce centimetre-sized cockades and streaks surrounded by a biotite-
266 free, quartzofeldspathic halo; cordierite includes numerous quartz grains but is free of
267 feldspars, and overall presents characteristics similar to late-magmatic cordierite reported
268 from other S-type granites (e.g. Barbey et al., 1999). It also contains a few grains of
269 tourmaline. These structures overprint the syn-magmatic fabric carried by biotite, indicating
270 that cordierite grew at its expense at the end of the crystallization sequence.
271 Cordierite is deeply retrogressed into pinite and we were not able to obtain reliable major
272 element composition. Tourmaline shows X_{Mg} values around 0.48–0.50.
273
274 *4.5. Feldspars*
275 They correspond dominantly to K-feldspar and in lesser proportion to sodic plagioclase.
276 Plagioclase occurs as small euhedral to subhedral grains (mostly ca. 0.1–0.2 mm), scattered in
277 the matrix (Fig. 13a), forming locally glomerophyric aggregates (Fig. 13b), or overgrown on
278 quartz grains (Fig. 13f). Unaltered grains correspond to oligoclase/andesine ($An_{\leq 25}$; Fig. 10a).
279 Albite is a widespread secondary mineral phase, which occurs as thin rims around
280 plagioclase, or veinlets along grain boundaries between the matrix K-feldspar grains (Fig.
281 13a); it also replaces primary plagioclase crystals, forming patchy zoning in association with
282 K-feldspar and muscovite (Fig. 13c, f).
283 K-feldspar, the main interstitial phase, may occur as subhedral to euhedral crystals (Fig.
284 13d), but in most cases, it is anhedral and forms an almost equilibrated mosaic between quartz
285 and plagioclase grains (Fig. 13a). It may be perthite-free, but more commonly contains
286 variable proportions of exsolutions, some crystals being strongly perthitic (Fig. 13e). It also
287 occurs as a secondary phase forming thin rims around plagioclase crystals (Fig. 13f), or
288 patches partly replacing them. K-feldspar has a composition ranging from $Or_{74}Ab_{25}An_{01}$ solid
289 solution for the magmatic feldspar to the orthoclase end-member for the secondary one (Fig.

10c). Within a single grain, the composition varies very weakly, with Na_2O contents ranging from 0.3 to 1.2 wt.%. Analysis of a few exsolutions shows An-rich compositions ($Or_{16–26}Ab_{61–68}An_{14–16}$).

5. Discussion

Whole-rock geochemical data show that the studied alkali-feldspar granite derives from parent magma generated by partial melting of an old recycled continental crust, in agreement with the regional geodynamic reconstruction (Skrzypek et al., 2014). Its composition is close to that of S-type felsic rocks used in crystallization experiments (e.g. Clemens and Birch, 2012; Scaillet et al., 1995) (Table 1), even though its rather high peraluminosity could be partly related to the alteration of feldspars in sericite. However, the small compositional heterogeneities (Si, Fe, REE, Th, U, Nb and Ta) observed within and in between units, and their distinct textures seemingly implying distinct melt water contents (see below, section 5.3), suggest that the three units derive from three different magma batches with distinct water content, and probably represent different stages of differentiation of a common parent magma.

5.1. Crystallization sequence

Defining the sequence of crystallization is not straightforward from textural relationships. Inclusion of garnet as minute grains in plagioclase and as more or less retrogressed grains in biotite suggests that it is probably one of the first phase on the liquidus. The common occurrence of plagioclase as euhedral crystals overgrown on quartz grains, or in interstitial position between them suggest that this phase started crystallizing after quartz. The appearance of biotite postdates quartz, though their relationships are a little more complex in detail (see next subsection). Timing of crystallization of biotite and plagioclase is to some extent ambiguous. The presence of scarce plagioclase inclusions within biotite could suggest

315 that the former started to crystallize first; however, it is more likely that these two phases
316 followed closely each other. K-feldspar, the last magmatic phase to crystallize, mostly forms a
317 granoblastic mosaic of crystals embedding all the other minerals, even though it can be
318 locally euhedral, suggesting local crystallization without interference with neighbouring
319 grains. This sequence ends with the scarce growth of cordierite (± tourmaline) at the expense
320 of biotite, and then partial subsolidus reequilibration (albite, chlorite, etc.).
321 From previous works (Latouche et al., 1992; Rey et al., 1989; Skrzypek et al., 2012) and
322 U–Pb zircon data indicating that the alkali-feldspar granite predates the Central Vosges
323 granite association (Supplementary material SM.1), a poorly constrained 200–500 MPa range
324 could be envisaged for the conditions of emplacement. Temperatures estimated from zircon
325 saturation thermometry (740–800°C) are too low to be considered those of the magma at the
326 time of its emplacement, especially since part of the zircon is inherited. Although the high
327 variance of the phase assemblage does not allow a precise reconstruction of the P–T
328 conditions of emplacement, we attempted a comparison with the experimental results
329 obtained by Clemens and Birch (2012) on the Rubicon Ignimbrite, compositionally close to
330 our granite. From their T–$X^{Fl}H_2O$ phase diagrams it appears that the early crystallization of
331 garnet in the absence of orthopyroxene, cordierite and biotite implies crystallization pressure
332 around 500 MPa from hydrated magma, and this seems to occur in a restricted field (800 < T
333 < 880°C, 0.4 < $X^{Fl}H_2O$ < 0.8). Their results also indicate that (i) the stability field of
334 cordierite expands widely with decreasing pressures, and (ii) feldspars are the late phases to
335 appear. Comparing our sequence of crystallization with these experimental data could suggest
336 that crystallization started at pressure around 500 MPa from a magma with significant melt
337 water content, but took place mainly at lower pressure to account for the early appearance of
338 quartz and the late crystallization of cordierite. In fact, we should expect cordierite to appear
339 earlier in the sequence, which is not the case; it cannot be excluded that its absence in the first

steps could be due to inhibited nucleation as observed in experiments (Clemens and Birch, 2012). A last point is that the onset of plagioclase crystallization occurred before biotite and K-feldspar, which is at odds with the experimental results showing that plagioclase is late in the crystallization sequence. Nevertheless, in experiments on Himalayan leucogranite (Scaillet et al., 1995) also compositionally close to our granite, plagioclase appears early, suggesting that minor compositional differences may lead to inversion in the crystallization order.

5.2. Significance of the textures of quartz and biotite

From the cathodoluminescence properties of quartz we consider that the bluish cores and reddish overgrowths of quartz grains represent two successive growth stages. Indeed, studies of quartz from igneous rocks (Götze et al., 2001; and references therein) suggest that Al (and possibly Ti) could play a role in the blue emission component, whereas the red component (often observed in rims and cracks of crystals) would be related to lattice defects. Quartz-1 (bluish cores) predates biotite and corresponds to both skeletal crystals and rounded to subhedral grains with a regular to wavy outline. Quartz-2 (reddish overgrowths) and biotite crystallized synchronously as indicated by their symplectitic relationships (Fig. 7f). Growth of quartz-2 resulted in the formation of rounded to euhedral grains from the skeletal cores, as well as in grain coalescence and equilibrated textures by grain feeding along boundaries from the melt. On the whole, the sharp contact between the two generations of quartz shown by CL and their distinct textural position mark an abrupt change in growth conditions. This is distinct from what is observed in olivine wherein P enrichment appears to reflect a continuous decay in growth rate (e.g. Welsch et al., 2014).

The skeletal shapes of quartz-1 can be interpreted in two ways, either dissolution or disequilibrium growth. Dissolution appears highly unlikely even though adiabatic

365 decompression can lead to remelting of early crystallized assemblages (Johannes and Holtz,
366 1996), and this for two main reasons. First, quartz dissolution experiments in rhyolitic melts
367 (Donaldson and Henderson, 1988) show that this process leads to round corners and edges,
368 and overall to more compact morphologies, but not to sharp crystal edges as we observe (see
369 also Swanson and Fenn, 1986). Secondly, if we rely on the phase relationships of the Rubicon
370 ignimbrite, it appears that for a magma (500 MPa, 850°C, $X^{Fl}H_2O = 0.5$) ascending
371 adiabatically, quartz starts to crystallize only down to 200 MPa, i.e. close to the level of
372 emplacement. We rather consider that the skeletal shapes result from diffusion-controlled
373 growth as observed in crystallization experiments at high undercooling (Swanson and Fenn,
374 1986; MacLellan and Trembath, 1991). In addition, variation of the degree of undercooling
375 during emplacement could account for the occurrence of both skeletal habits (early high
376 supersaturation) and rounded grains with smooth outlines (subsequent decreasing
377 undercooling). In any case, the skeletal shape of quartz-1, whatsoever resulting from
378 dissolution or disequilibrium crystallization, can be considered as primary disequilibrium
379 textures preserved behind the apparent "coarse-grained" texture.
380 It is worth of note that the CL image of Fig. 8b contains a quartz grain showing a hollow
381 core with arms radiating towards its centre. This grain presents a sub-hexagonal section (faces
382 are easily recognizable), thus not far from being orthogonal to the *c* axis. This disposition
383 seems therefore to indicate that the arms are radial with respect to this axis, which is in
384 agreement with the experimental results of Swanson and Fenn (1986).
385 Looking at the quartz grain size in the three units (Fig. 8), it appears that its distribution in
386 Unit-1 and Unit-2 are quite comparable, differing mainly by the average grain size and the
387 proportion of larger grains (~ 15 % in Unit-1 vs. 30–55 % in Unit-2). This may simply result
388 from distinct cooling, due to the thermal state of the host rock. Compared to Unit-2, the
389 histogram of Unit-3 differs by a limited population of small grains (≤ 0.1 mm) and a very

restricted population of larger grains (~ 25 % ≥ 0.3 mm) which is closer to that of Unit-1. Although we cannot fully discard cutting effects, we consider that two processes may account for this peculiar distribution. Firstly, the limited amount of small grains suggests coarsening by Ostwald ripening probably mainly in favour of medium sizes since this process seems to be only effective for small sizes (Cabane et al., 2001). This also implies that there was no creation of new grains and, thus, that the nucleation of quartz has not been continuous. Secondly, the restricted population of larger grains implies that coarsening was rapidly impeded.

Textural relationships indicate that biotite postdates quartz-1 and possibly plagioclase, while it is coeval with quartz-2. Furthermore, variation of its size and morphology from one unit to the other suggests distinct nucleation and growth rates, and therefore distinct magma supersaturation in each unit. More particularly, the large size of biotite crystals in Unit-3 and their tendency to form radiating clusters (nucleation of several grains at a single site) implies very limited nucleation. This precludes in situ differentiation of the three units from a unique magma batch by fractional crystallization. We note that the morphology of biotite from Unit-3 resembles those of biotite from stockscheider pegmatites (see for example Haapala and Lukkari, 2005; their Fig. 3c). However, the absence, in this unit and in the whole granite body as well, of rhythmic mineralogical laminations, feldspar and quartz segregation, inward gradual increase of crystal size and unidirectional growth texture from walls indicates that the studied granite cannot be equated to pegmatite (for pegmatite features, see London and Morgan, 2017), even though similar process may have been at work.

5.3. A possible crystallization scenario

Some experimental results may help us in building an appropriate scenario. (1) As pointed out by Swanson (1977) and Swanson and Fenn (1986), the nucleation of quartz is an abrupt

process at high rates in granitic melts. (2) Ostwald ripening of quartz grains seems to be an active process only at the end of nucleation event, becoming negligible when grains reach millimetre size (Cabane et al., 2001). (3) At high undercooling (i.e. high supersaturation conditions), crystal habit evolves towards skeletal and dendritic shapes, with radial growth patterns (e.g. London, 2005; and references therein, for silicic rocks). More specifically, London and Morgan (2017) show in their experiments that limited undercooling leads to fine-grained disseminated crystals, whereas at high undercooling crystal evolves towards skeletal and radiating morphologies.

Considering that the three units correspond to three distinct batches from a common source, emplaced at the same level in the crust, the only two parameters that are likely to vary to account for distinct supersaturation in each unit at the site of emplacement, are (i) the temperature of the surrounding rocks, owing to the fact that the Unit-1 was emplaced in colder host-rocks while the Unit-2 and Unit-3 are nested in the preceding ones; and (ii) the volatile content of the melt and extent of degassing that may differ from one magma batch to the other. We therefore propose a crystallization scenario in three main steps.

(1) *The first step* common to all units corresponds to the onset of crystallization of garnet from a hydrated silicic peraluminous melt under pressures of ca. 500 MPa to avoid early crystallization of orthopyroxene or cordierite. It is not unlikely that this happened in an evolving intermediate magma chamber that fed the successive injections (Fig. 14a).

(2) *The second step* corresponds to magma emplacement and the onset of crystallization of quartz, followed by plagioclase, biotite and K-feldspar. It is this step that imprints the textural characteristics of the three units. Decompression and cooling during magma ascent may have led to undercooled melt, resulting in low nucleation and rapid growth of skeletal quartz-1 when magma reached its site of emplacement (Fig. 14b). The subsequent evolution has to be discussed for each unit, separately (Fig. 14c, d).

The first batch of magma (Unit-1) was emplaced in a colder environment. This induced rapid cooling and significant undercooling, which led to high nucleation of quartz followed by limited but to some extent protracted growth resulting in a certain heterogeneity towards larger grain sizes. The crystallization of quartz led in turn to significant supersaturation with respect to plagioclase and biotite. An important peak of nucleation followed by limited growth gave a homogeneous population of small-sized biotite crystals.

The next magma injection (Unit-2) intruded Unit-1, i.e. an environment hotter than for the first batch. This led to moderate cooling rate and undercooling, lowered nucleation but increased growth of quartz, with limited Ostwald ripening; the result is a more heterogeneous population of larger quartz grains. The subsequent crystallization of biotite followed the same evolution as quartz, also resulting in a heterogeneous population of larger crystals. The heterogeneity and larger size of both quartz and biotite along with the higher amount of deformation recorded in this unit seem to suggest a longer duration of solidification. Overall, Unit-1 and Unit-2 show crystallization process no so much different from common igneous rocks.

The third batch of magma (Unit-3) is distinguished by a more homogeneous population of quartz compared to Unit-2, suggesting that both nucleation and coarsening were to some extent hindered, and therefore that crystallization process has been limited in time. This needs conditions distinct from those operating in the former units, i.e. a process other than cooling rate; this is also supported by the absence of unidirectional growth pattern, thus precluding a significant role of thermal contrast between Unit-2 and Unit-3. The best way to explain these features is to invoke a sudden drop of water pressure by degassing of a magma with higher melt water content, triggering high degree of undercooling by shifting the liquidus of the system, which makes growth and nucleation more rapid. However, this is counteracted by increase in the viscosity of the melt, slowing down diffusion. This may also account for

reducing nucleation of biotite and thus for its high growth rate and dendritic habit. The low diffusivity may also be the cause of biotite crystals forming radiating clusters (nucleation of several grains at a single site).

The end of this step corresponds to the onset of crystallization of K-feldspar (even though it is not possible to determine precisely when this phase started crystallizing), forming mostly a mosaic of equilibrated grains. Note that crystallization of biotite and feldspars maintained in all units the supersaturation of the residual melt in silica and led concomitantly to the crystallization of quartz-2 overgrowing former quartz grains and filling pore spaces.

(3) *The last step* common to all three units corresponds to the local growth of cordierite (± tourmaline); and, finally, to subsolidus fluid-assisted reequilibration (albite, chlorite, etc.).

We are aware that this scenario is very qualitative, but linking it to quantitative assessment of nucleation and growth rates as functions of undercooling is not really possible considering the present state of available experimental studies.

6. Conclusions

(1) The studied S-type alkali-feldspar granite was emplaced as three nested units. The crystallization sequence started with garnet, then proceeded with quartz, plagioclase, biotite and K-feldspar, and ended with cordierite. In Unit-1, quartz and biotite are small-sized; in Unit-2, they are coarser-grained forming more a heterogeneous population; and in Unit-3, quartz forms a homogeneous population of smaller grains than in Unit-2, whereas biotite is significantly larger in size (up to 8.5 cm).

(2) Quartz occurs mostly as subhedral to euhedral grains, even though more complex shapes are observed. Cathodoluminescence imaging reveals that quartz grains consist of bluish rounded or skeletal core filled and/or surrounded by reddish overgrowth. Biotite is

poikilitic in all units including mostly quartz grains but also plagioclase and garnet; in unit 3, biotite crystals are arranged radially, have dendritic habits and also skeletal cores.

(3) The variability in size and morphology of quartz and biotite is interpreted in terms of variable undercooling related to variable temperature of the host-rocks and to more or less intense degassing due to magma batches characterized by variable melt water content.

(4) Overall, this study illustrates that behind the common "coarse-grained" texture of quartz in granite, subsist primary disequilibrium crystallization textures. This probably results from a favourable situation in which the thermal evolution has not totally erased the initial crystallisation textures. However, it is not impossible that majority of granites kept relics that will not be visible without examination under cathodoluminescence. Finally, the claim of Welsch et al. (2013) that all euhedral olivine crystals in basaltic rocks are initially dendritic or skeletal could also be applicable to other minerals and rock types.

Acknowledgements

This work was supported by the TelluS Program of CNRS/INSU. We thank the Centre Terrae Genesis for assistance in field work and sample polishing, Alexandre Flammang for thin section preparation, Emmanuel Davy for zircon separation, and Olivier Rouer for assistance with electron microprobe analyses. We are indebted to M. Holness, D. London and O. Müntener for their helpful comments on an earlier version of this paper. Constructive reviews by J. Hammer and J. Vander Auwera are gratefully acknowledged.

References

Ackerson, M.R., Mysen, B.O., Tailby, N.D., Watson, E.B., 2018. Low-temperature crystallization of granites and the implications for crustal magmatism. Nature doi.org/10.1038/s41586-018-0264-2.

514 Ahmed, S.A.E., 2011. The origin of quartz glomerocrysts: insights from the rhyolite dike at
515 Medicine Park, Oklahoma. Masters Theses, 56p.
516 http://scholarsmine.mst.edu/masters_theses/5032.
517 Almeev, R.R., Holtz, F., Koepke, J., Parat, F., Botcharnikov, R.E., 2007. The effect of H_2O
518 on olivine crystallization in MORB: Experimental calibration at 200 MPa. American
519 Mineralogist 92, 670-674.
520 Ballouard, C., Poujol, M., Boulvais, P., Branquet, Y., Tartèse, R., Vigneresse, J.L., 2016. Nb-
521 Ta fractionation in peraluminous granites: A marker of the magmatic-hydrothermal
522 transition. Geology 44, 231-234.
523 Barbey P., Marignac C., Montel J.M., Macaudière J., Gasquet D., Jabbori J., 1999. Cordierite
524 growth textures and the conditions of genesis and emplacement of crustal granitic magmas:
525 the Velay granite complex (Massif Central, France). Journal of Petrology 40(9), 1425-
526 1441.
527 Bau, M., 1996. Controls on the fractionation of isovalent trace elements in magmatic and
528 aqueous systems: evidence from Y/Ho, Zr/Hf, and lanthanide tetrad effect. Contributions
529 to Mineralogy and Petrology 123, 323-333.
530 Cabane, H., Laporte, D., Provost, A., 2001. Experimental investigation of the kinetics of
531 Ostwald ripening of quartz in silicic melts. Contributions to Mineralogy and Petrology 142,
532 361-373.
533 Cashman, K.V., Marsh, B.D., 1988. Crystal size distribution (CSD) in rocks and the kinetics
534 and dynamics of crystallization II: Makaopuhi lava lake. Contributions to Mineralogy and
535 Petrology 99(3), 292-305.
536 Cawthorn, R.G., 1996. Layered intrusions. Elsevier, Amsterdam, 531p.

537 Clemens, J.D., Birch, W.D., 2012. Assembly of a zoned volcanic magma chamber from
538 multiple magma batches: The Cerberean Cauldron, Marysville Igneous Complex,
539 Australia. Lithos 155: 272-288.
540 Decitre, S., Gasquet, D., Marignac, C., 2002. Genesis of orbicular granitic rocks from the
541 Ploumanac'h Plutonic Complex (Brittany, France). European Journal of Mineralogy 14,
542 715-731.
543 Donaldson, C.H., 1974. Olivine crystal types in harrisitic rocks of the Rhum pluton and in
544 Archean spinifex rocks. Geological Society of America Bulletin 85, 1721-1726.
545 Donaldson, C.H., 1976. An experimental investigation of olivine morphology. Contributions
546 to Mineralogy and Petrology 57(2), 187-213.
547 Donaldson, C.H.,1982. Spinifex-textured komatiites: a review of textures, compositions and
548 layering. In: Arndt, N.T., Nisbet, E.G. (Eds) Komatiites. Allen and Unwin, London, pp.
549 213-244.
550 Donaldson, C.H., Henderson, C.M.B., 1982. Interpretation of round embayment in quartz
551 crystals. Mineralogical Magazine 52, 27-33.
552 El Bouseily, A.M., El Sokkary, A.A., 1975. The relation between Rb, Ba and Sr in granitic
553 rocks. Chemical Geology 16, 207-219.
554 Evensen, N.M., Hamilton, M.J., O'Nions, R.J., 1978. Rare-earth abundances in chondritic
555 meteorites. Geochimica et Cosmochimica Acta 42, 1199-1212.
556 Faure, F., Arndt, N., Libourel, G., 2006. Formation of spinifex texture in komatiites: an
557 experimental study. Journal of Petrology 47, 1591-1610.
558 Faure, F., Trolliard, G., Nicollet, C., Montel, J. M., 2003. A developmental model of olivine
559 morphology as a function of the cooling rate and the degree of undercooling. Contributions
560 to Mineralogy and Petrology 145, 251-263.

561 Fluck, P., Piqué, A., Schneider, J.L., Whitechurch, H., 1991. Le socle vosgien. Science
562 Géologique Bulletin 44, 207-235.
563 Frindt, S., Haapala, I., 2004. Anorogenic Gross Spitzkoppe granite stock in central western
564 Namibia: Part II. Structures and textures indicating crystallization from undercooled melt.
565 American Mineralogist 89, 857-866.
566 Frost, B.R., Barnes, C.G., Collins, W.J., Arculus, R.J., Ellis, D.J., Frost, C.D., 2001. A
567 geochemical classification for granitic rocks. Journal of Petrology 42, 2033-2048.
568 Gillespie, M.R., Styles, M.T., 1999. BGS Rock Classification Scheme. Volume 1:
569 Classification of igneous rocks. British Geological Survey Research Report (2nd edition)
570 RR 99–06, 52p.
571 Götze, J., Plötze, M., Habermann, D., 2001. Origin, spectral characteristics and practical
572 applications of the cathodoluminescence (CL) of quartz–α review. Mineralogy and
573 Petrology 71(3-4), 225-250.
574 Haapala, I., Lukkari, S., 2005. Petrological and geochemical evolution of the Kymi stock, a
575 topaz granite cupola within the Wiborg rapakivi batholith, Finland. Lithos 80, 347-362.
576 Higgins, M.D., 2011. Textural coarsening in igneous rocks. International Geology Review
577 53(3–4), 354-376.
578 Holness, M.B., 2005. Spatial constraints on magma chamber replenishment events from
579 textural observations of cumulates: The Rum Layered Intrusion, Scotland. Journal of
580 Petrology 46(8), 1585-1601.
581 Holness, M. B., Anderson, A. T., Martin, V. M., MacLennan, J., Passmore, E., Schwindinger,
582 K., 2007a. Textures in partially solidified crystalline nodules: a window into the pore
583 structure of slowly cooled mafic intrusions. Journal of Petrology 48(7), 1243–1264.

584 Holness, M.B., Nielsen, T.F.D., Tegner, C., 2007b. Textural maturity of cumulates: A record
585 of chamber filling, liquidus assemblage, cooling rate and large-scale convection in mafic
586 layered intrusions. Journal of Petrology 48(1), 141-157.
587 Holness, M.B., Tegner, C., Nielsen, T.F.D., Stripp, G., Morse, S.A., 2007c. A textural record
588 of solidification and cooling in the Skaergaard Intrusion, East Greenland. Journal of
589 Petrology 48(12), 2359-2377.
590 Irber, W., 1999. The lanthanide tetrad effect and its correlation with K/Rb, Eu/Eu*, Sr/Eu,
591 Y/Ho, and Zr/Hf of evolving peraluminous granite suites. Geochimica et Cosmochimica
592 Acta 63, 489-508.
593 Ivanov, I.M., Grozdanov, L.A., 2001. Biotite in the granitic pegmatites in the deposit of
594 Smilovene, Koprivshtitsa region. Comptes Rendus de l'Académie bulgare des Sciences
595 54(4), 59-64.
596 Johannes, W., Holtz, F., 1996. Petrogenesis and Experimental Petrology of Granitic Rocks.
597 Springer-Verlag, Berlin, Heidelberg. 335 pp.
598 Jahn, B.M., Wu, F., Capdevila, R., Martineau, F., Zhao, Z., Wang, Y., 2001. Highly evolved
599 juvenile granites with tetrad REE patterns: the Woduhe and Baerzhe granites from the
600 Great Xing'an Mountains in NE China. Lithos 59, 171-198.
601 Latouche, L., Fabriès, J., Guiraud, M., 1992. Retrograde evolution in the Central Vosges
602 mountains (north-eastern France): implications for the metamorphic history of high-grade
603 rocks during the Variscan orogeny. Tectonophysics 205, 387-407.
604 Lesher, C.E., Walker, D., 1988. Cumulate maturation and melt migration in a temperature
605 gradient. Journal of Geophysical Research, Solid Earth 93, 10295-10311.
606 Libourel, G., Portail, M., 2018. Chondrules as direct thermochemical sensors of solar
607 protoplanetary disk gas. Science Advances 4(7), eaar3321.

608 Lofgren, G., 1974. An experimental study of plagioclase crystal morphology. American
609 Journal of Science 274, 243-273.
610 Lofgren, G., 1980. Experimental studies on the dynamic crystallization of silicate melts. In:
611 Hargraves, R.B. (Ed.) Physics of magmatic processes, Princeton University Press, New
612 Jersey, pp. 487-551.
613 Lofgren, G.E., Donaldson, C.H., 1975. Curved branching crystals and differentiation in comb-
614 layered rocks. Contributions to Mineralogy and Petrology 49, 309-319.
615 London, D., 2005. Granitic pegmatites: an assessment of current concepts and directions for
616 the future. Lithos 80, 281-303.
617 London, D., 2009. The origin of primary textures in granitic pegmatites. Canadian
618 Mineralogist 47(4), 697-724.
619 London, D., Morgan, G.B., 2017. Experimental crystallization of the Macusani obsidian, with
620 applications to lithium-rich granitic pegmatites. Journal of Petrology 58(5), 1005-1030.
621 MacLellan, H.E., Trembath, L.T., 1991. The role of quartz crystallization in the development
622 and preservation of igneous texture in granitic rocks; experimental evidence at 1 kbar.
623 American Mineralogist 76, 1291-1305.
624 Marsh, B.D., 1988. Crystal size distribution (CSD) in rocks and the kinetics and dynamics of
625 crystallization. I. Theory. Contributions to Mineralogy and Petrology 99, 277-291.
626 Médard, E., Grove, T.L., 2008. The effect of H_2O on the olivine liquidus of basaltic melts:
627 Experiments and thermodynamic models. Contributions to Mineralogy and Petrology 155,
628 417-432.
629 Milman-Barris, M.S., Beckett, J.R., Baker, M.B., Hofman, A.E., Morgan, Z., Crowley, M.R.,
630 Vielzeuf, D., Stolper, E., 2008. Zoning of phosphorus in igneous olivine. Contributions to
631 Mineralogy and Petrology 155, 739-765.

632 Müller, A., Kronz, A., Breiter, K., 2002. Trace elements and growth patterns in quartz: a
633 fingerprint of the evolution of the subvolcanic Podlesí Granite System (Krusné hory Mts.,
634 Czech Republic). Bulletin of the Czech Geological Survey 77(2), 135-145.
635 Rey, P., Burg, J. P., Lardeaux, J.M., Fluck, P., 1989. Evolutions métamorphiques contrastées
636 dans les Vosges orientales : témoins d'un charriage dans la chaîne varisque. Comptes
637 Rendus de l'Académie des sciences, Paris, Série 2, 309, 815-821.
638 Scaillet, B., Pichavant, M., Roux, J., 1995. Experimental crystallization of leucogranite
639 magmas. Journal of Petrology 36, 663-705.
640 Seitz, S., Putlitz, B., Baumgartner, L.P., Escrig, S., Meibom, A., Bouvier, A.S., 2016. Short
641 magmatic residence times of quartz phenocrysts in Patagonian rhyolites associated with
642 Gondwana breakup. Geology 44, 67-70.
643 Shannon, J.R., Walker, B.M., Carten, R.B., Geraghty, E.P., 1982. Unidirectional solidification
644 textures and their significance in determining relative ages of intrusions at the Henderson
645 Mine, Colorado. Geology 10, 293-297.
646 Skrzypek, E., Schulmann, K., Tabaud, A.S., Edel, J.B., 2014. Palaeozoic evolution of the
647 Variscan Vosges mountains. In: Schulmann, K., Martìnez Catalán, J.R., Lardeaux, J.M.,
648 Janoušek, V., Oggiano, G. (Eds), The Variscan Orogeny: Extent, Timescale and the
649 Formation of the European Crust. Geological Society, London, Special Publications 405,
650 45-75.
651 Smillie, R.W., Turnbull, R.E., 2014. Field and petrographical insight into the formation of
652 orbicular granitoids from the Bonney Pluton, southern Victoria Land, Antarctica.
653 Geological Magazine 151, 534-549.
654 Streckeisen, A., Le Maitre, R.W., 1979. A chemical approximation to the modal QAPF
655 classification of the igneous rocks. Neues Jahrbuch für Mineralogie, Abhandlungen 136,
656 169-206.

657 Sun, S.-S., McDonough, W.F., 1989. Chemical and isotopic systematics of oceanic basalts:
658 implications for mantle composition and processes. In: Saunders, A.D., Norry, M.J. (Eds),
659 Magmatism in the Ocean Basins. Geological Society, London, Special Publications 42,
660 313-345.
661 Swanson, S. E., 1977. Relation of nucleation and crystal-growth rate to the development of
662 granitic textures. American Mineralogist 62, 966–978.
663 Swanson, S.E., Fenn, P.M., 1986. Quartz crystallization in igneous rocks. American
664 Mineralogist 71, 331-342.
665 Tabaud, A. S., Janoušek, V., Skrzypek, E., Schulmann, K., Rossi, P., Whitechurch, H., Guerrot,
666 C. & Paquette, J. L., 2015. Chronology, petrogenesis and heat sources for successive
667 Carboniferous magmatic events in the Southern–Central Variscan Vosges Mts (NE France).
668 *Journal of the Geological Society* 172, 87–102.
669 Vernon, R.H. 1985. Possible role of superheated magma in the formation of orbicular
670 granitoids. Geology 13, 843-845.
671 Watson, E.B., Harrison, T.M., 1983. Zircon saturation revisited: temperature and composition
672 effects in a variety of crustal magma types. Earth and Planetary Science Letters 64, 295-
673 304.
674 Watt, G.R., Wright, P., Galloway, S., McLean, C., 1997. Cathodoluminescence and trace
675 element zoning in quartz phenocrysts and xenocrysts. Geochimica et Cosmochimica Acta,
676 61, 4337-4348.
677 Welsch, B., Faure, F., Famin, V., Baronnet, A., Bachèlery, P., 2013. Dendritic crystallization:
678 A single process for all the textures of olivine in basalts? Journal of Petrology 54, 539-574.
679 Welsch, B., Hammer, J., Hellebrand, E., 2014. Phosphorus zoning reveals dendritic
680 architecture of olivine. Geology, 42(10), 867-870.

Whalen, J.B., Currie, K.L., Chappell, B.W., 1987. A-type granites: geochemical characteristics, discrimination and petrogenesis. Contributions to Mineralogy and Petrology 95, 407-419.

Xing, C.M., Wang, C.Y., Tan, W., 2017. Disequilibrium growth of olivine in mafic magmas revealed by phosphorus zoning patterns of olivine from mafic–ultramafic intrusions. Earth and Planetary Science Letters, 479, 108-119.

Figure captions

Fig. 1. Cross-section of the alkali-feldspar granite body, with sample location. Sample numbers refer to whole-rock and mineral analyses of Table 1 and Supplementary material SM.3.

Fig. 2. Unit-1. Size and morphology of biotite and quartzofeldspathic matrix. (a) Polished slab; (b) and (c) thin sections in plane polarized light and crossed nicols, respectively. (S_m = magmatic fabric; qz = quartz; fsp = feldspar; Kfs = K-feldspar; pl = plagioclase; bt = biotite; grt = garnet.)

Fig. 3. Unit-2. (a) Polished slab showing the size of biotite and its rough orientation along the syn-magmatic foliation (S_m). (b) Detail of biotite (blades) and garnet (dots) in a weakly foliated part of the unit (rough surface). (c) Polished slab showing an autolithic enclave wrapped by the foliation; note also the larger grain size of the lower part of the slab. (d) Thin section in plane polarized light showing the size and morphology of biotite, and texture of the quartzofeldspathic matrix.

706 **Fig. 4.** Unit-3. (a) and (b) Polished blocs showing the 3D organization of biotite plates. (c)
707 Polished slab showing the disposition of biotite and small rounded garnet grains. (c) Thin
708 section in plane polarized light showing the size and morphology of biotite and quartz.
709
710 **Fig. 5.** (a) Multi-element plot normalized to Primitive Mantle (Sun and McDonough, 1989).
711 (b) REE patterns normalized to chondrite (Evensen et al., 1978).
712
713 **Fig. 6.** Optical microphotographs of quartz. (a) Quartz grain with serrated edges. (b)
714 Equilibrated grain boundaries between quartz grains (see also Fig.7e). (c) Quartz film
715 (arrowed) along grain boundaries, in crystallographic continuity with the rounded quartz
716 grain. (d) Triangular extensions (arrowed) of quartz along feldspar-feldspar or feldspar-quartz
717 grain boundaries. (e) Re-entrants with tips (arrowed) tending to meet and form an inclusion.
718 (f) Interstitial quartz (arrowed) along grain boundaries between feldspar grains. (b), (c), (d)
719 and (e): Unit-3; (a) and (f): Unit-2.
720
721 **Fig. 7.** Cathodoluminescence images of quartz. (a) Elliptical cores (qz-1) with wavy or jagged
722 outlines, overgrown and welded by a second generation of quartz (qz-2); note the hollow core
723 of qz-1 to the right. (b) and (c) Cores showing branching arms. (d) Hollow crystal with
724 roughly radiating branches. (e) Coalescence of quartz grains welded by reddish quartz
725 overgrowth leading to an equilibrated grain assemblage. (f) Symplectitic quartz intergrowth
726 with biotite (arrowed); note that the symplectitic quartz overgrows a bluish quartz grain.
727 Other mineral phases are K-feldspar (blue and green), plagioclase (light brown), albite
728 (yellow) and biotite (dark). Scale bar: 100µm. (a), (b) and (e): Unit-3; (c) and (d): Unit-2.
729

730 **Fig. 8.** Size distribution of whole quartz grains in the three units. Note the greater size
731 heterogeneity in Unit-2. (aver. = average and standard deviation; n= number of grains
732 measured; diam. = diameter.)
733
734 **Fig. 9.** Microphotographs of garnet. (a) Euhedral garnet crystal (Unit-3). (b) Rounded garnet
735 grain included in plagioclase (Unit-2). (c) Retrogressed garnet crystal embedded in a biotite–
736 plagioclase groundmass (Unit-2).
737
738 **Fig. 10.** Mineral compositions: (a) Garnet in the Almandine–Pyrope–Spessartite+Grossularite
739 triangle; (b) Biotite in the Al^{VI} vs. (Fe + Mg) diagram; and (c) Feldspars in the Ab–Or–An
740 triangle (p = perthite). Compositions presented in these diagrams are given in the
741 Supplementary material SM.3.
742
743 **Fig. 11.** Morphology of biotite. (a) Strongly poikilitic aspect of biotite including numerous
744 quartz grains (Unit-3). (b) Branching, bifid, biotite crystal from Unit-2. (c) and (d) Dendritic
745 crystals from Unit-3. (e) Biotite showing hollow core (Unit-2). (f) Biotite with hollow core
746 filled with feldspar mainly (Unit-3).
747
748 **Fig.12.** Size distribution of biotite crystals in the three units (aver. = average and standard
749 deviation; n= number of grains measured; diam. = diameter).
750
751 **Fig. 13.** Morphology of feldspars. (a) Back-scattered electron microscopy (BSEM) image
752 showing a K-feldspar groundmass containing euhedral plagioclase crystals and rounded
753 quartz grains; note the presence of albite veinlets along K-feldspar grain boundaries and
754 around the euhedral plagioclase crystal. (b) BSEM image of glomerophyric texture of

plagioclase in a groundmass consisting of quartz (dark grey) and K-feldspar (light grey). (c) Optical microscopy image of plagioclase crystal showing a partly retrogressed core rimmed by albite and K-feldspar. (d) CL image showing the matrix forming euhedral to subhedral K-feldspar crystals (green to grey). (e) Optical microscopy image of a perthitic K-feldspar crystal. (f) CL image showing partial replacement of plagioclase crystals into albite or plagioclase rimmed with K-feldspar and albite (same grain as in c). (a), (b), (c), (e) and (f): Unit-3; (d): Unit-2.

Fig. 14. Interpretative sketch illustrating the main step of solidification of the alkali-feldspar granite (melt = light pink, garnet = red, quartz-1 = grey, quartz-2 = light grey, plagioclase = brown, biotite = black, primary K-feldspar = green, secondary albite = yellow, secondary K-feldspar = blue).

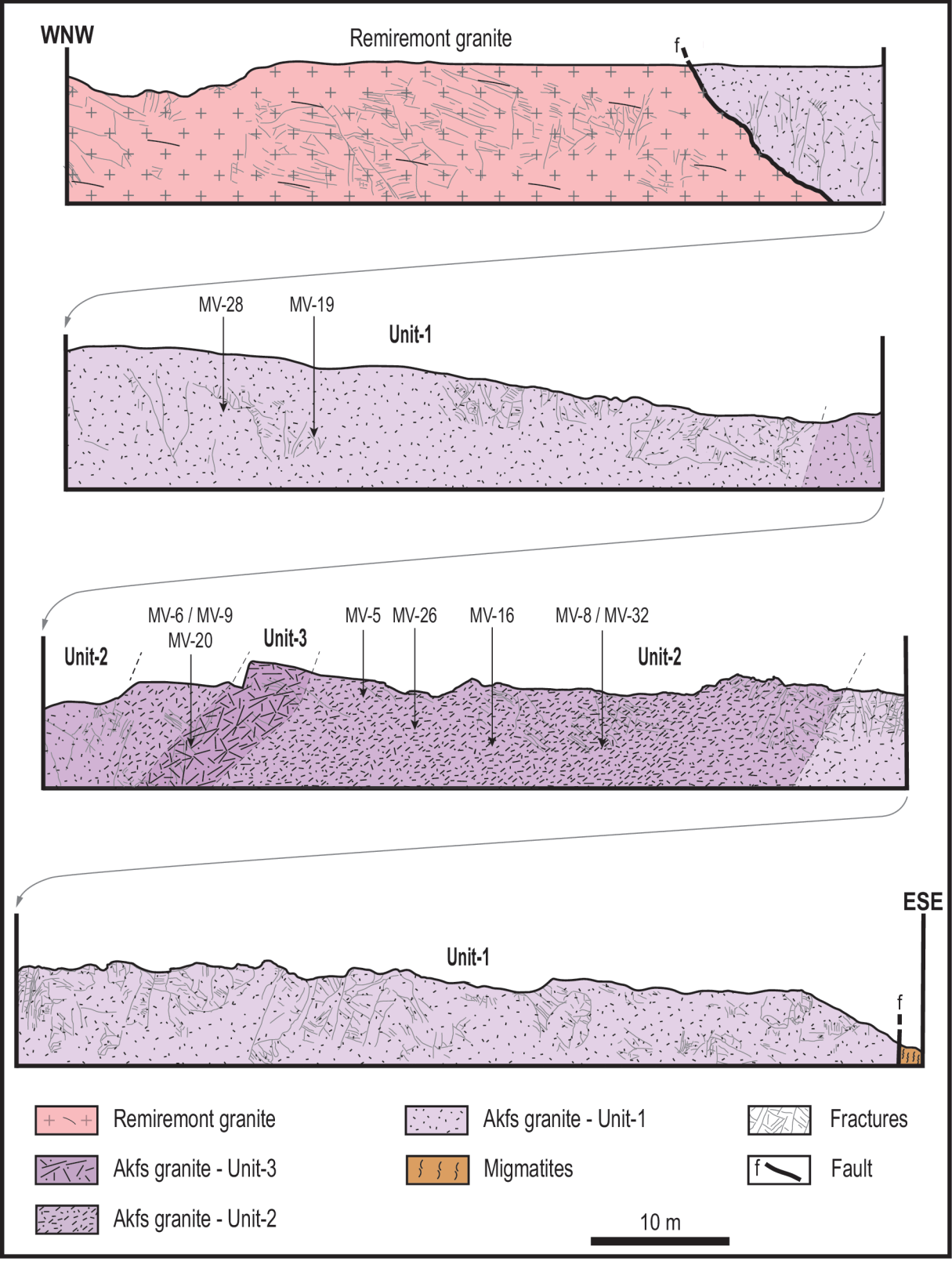
WNW
Remiremont granite
f
MV-28
MV-19
Unit-1
MV-6 / MV-9
MV-20
Unit-2
Unit-3
MV-5
MV-26
MV-16
MV-8 / MV-32
Unit-2
ESE
Unit-1
f
Remiremont granite
Akfs granite - Unit-3
Akfs granite - Unit-2
Akfs granite - Unit-1
Migmatites
Fractures
f
Fault
10 m

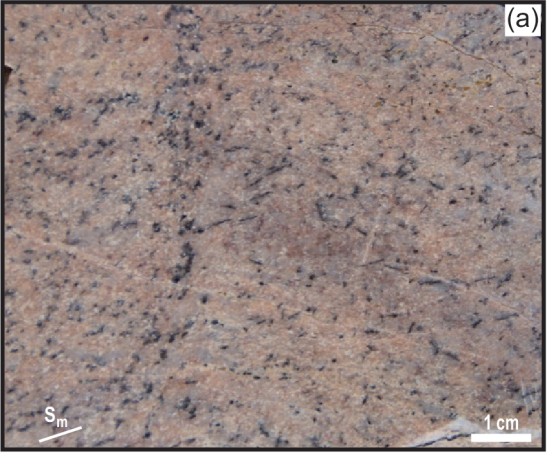
(a)
S_m
1 cm

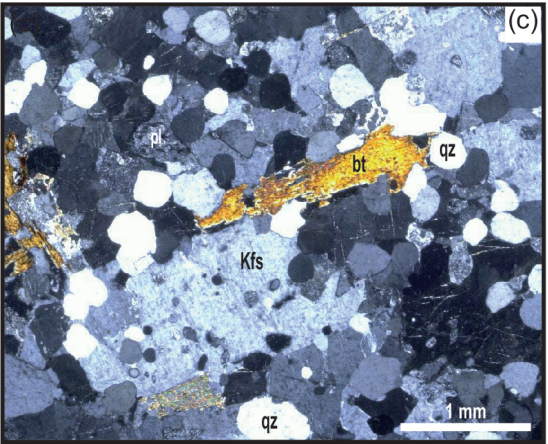
(c)
pl
bt
qz
Kfs
qz
1 mm

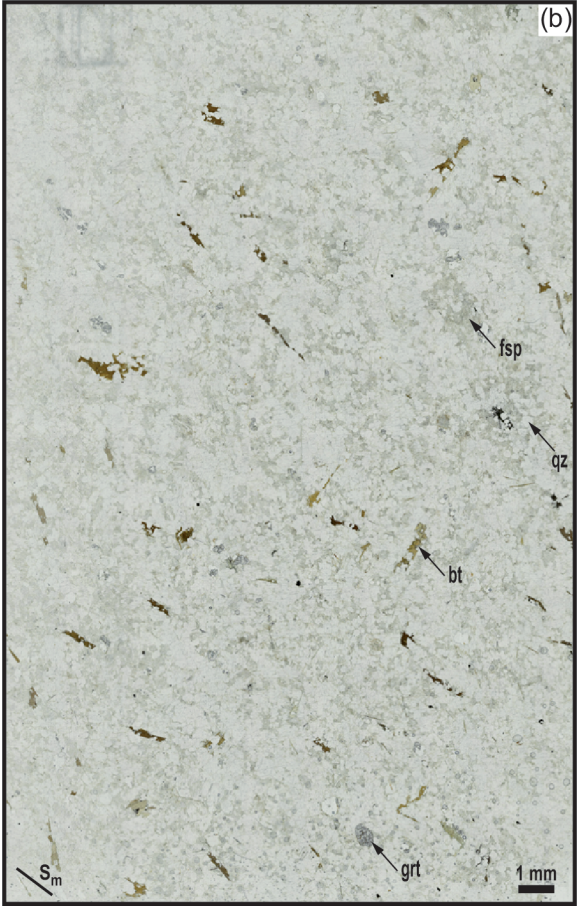
(b)
fsp
qz
bt
grt
S_m
1 mm

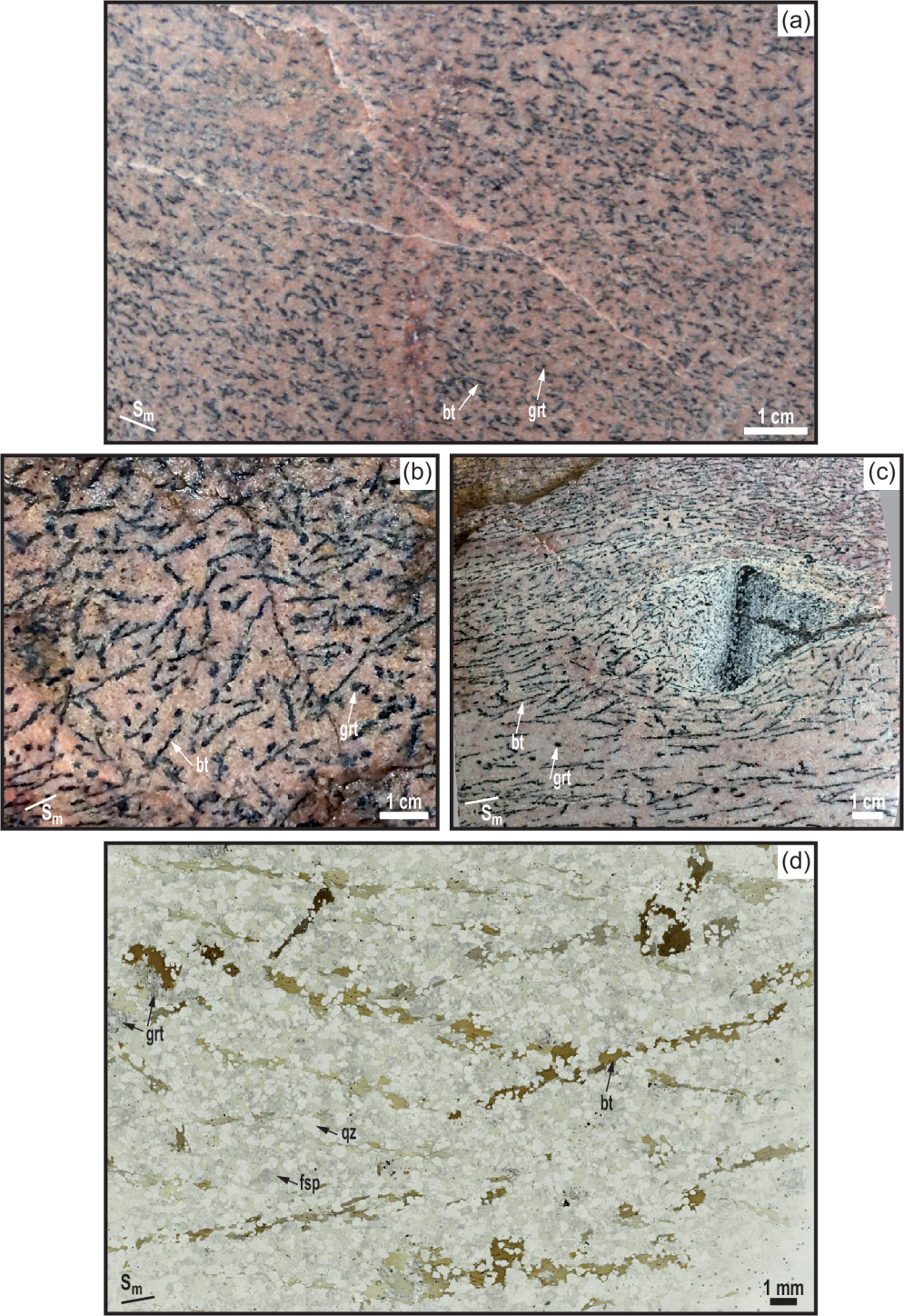
(a)
Sm
bt
grt
1 cm
(b)
grt
bt
Sm
1 cm
(c)
bt
grt
Sm
1 cm
(d)
grt
bt
qz
fsp
Sm
1 mm

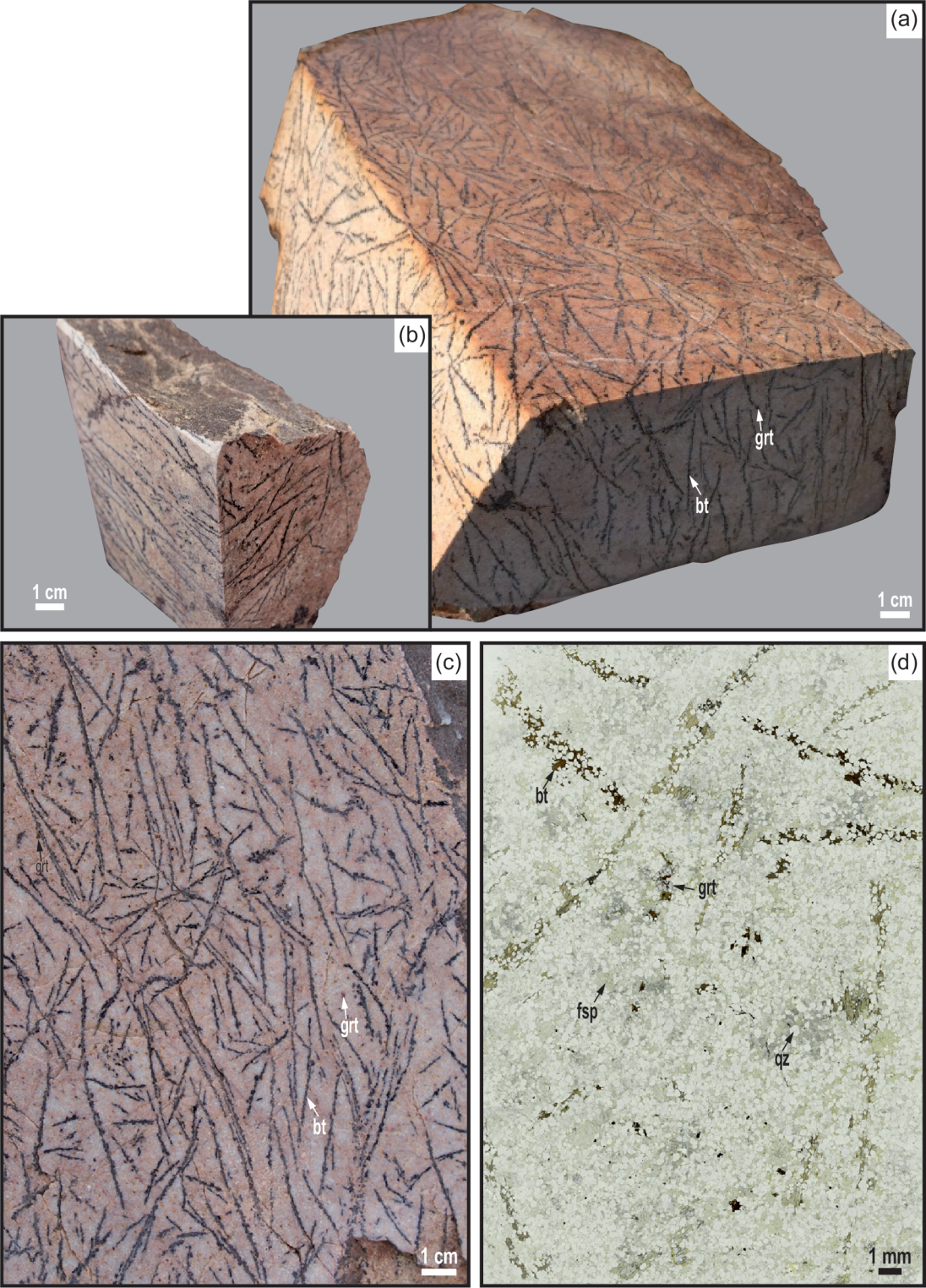
(a)
grt
bt
1 cm
(b)
1 cm
(c)
grt
grt
bt
1 cm
(d)
bt
grt
fsp
qz
1 mm

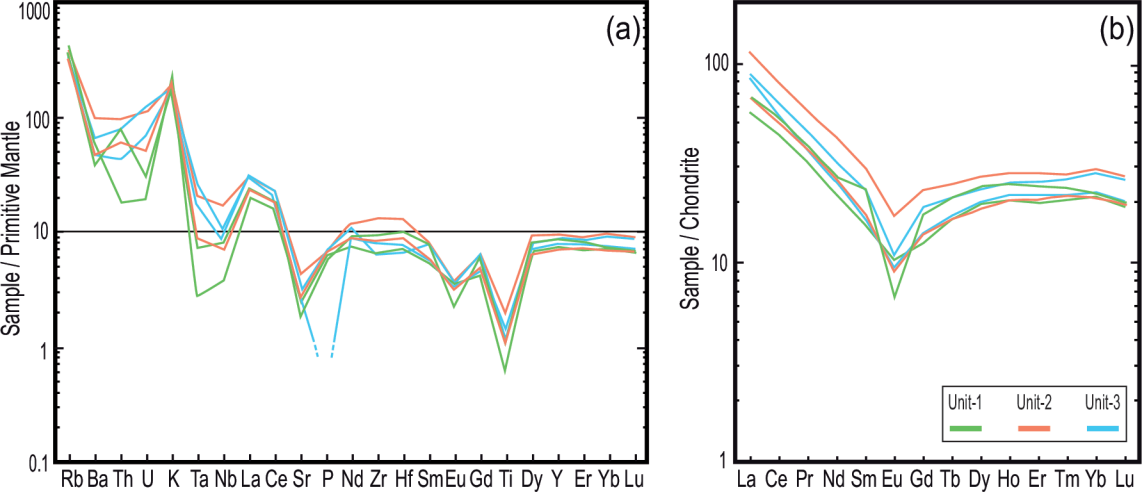
(a)
Sample / Primitive Mantle
1000
100
10
1
0.1
Rb Ba Th U K Ta Nb La Ce Sr P Nd Zr Hf Sm Eu Gd Ti Dy Y Er Yb Lu
(b)
Sample / Chondrite
100
10
1
La Ce Pr Nd Sm Eu Gd Tb Dy Ho Er Tm Yb Lu
Unit-1
Unit-2
Unit-3

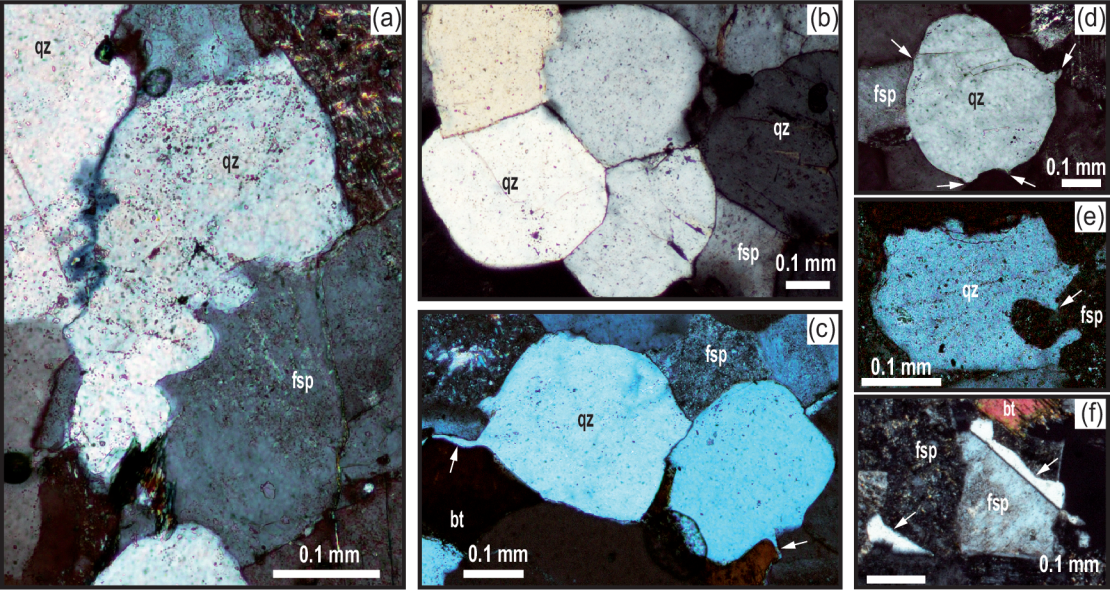
(a)
qz
qz
fsp
0.1 mm
(b)
qz
qz
fsp
0.1 mm
(c)
fsp
qz
bt
0.1 mm
(d)
fsp
qz
0.1 mm
(e)
qz
fsp
0.1 mm
(f)
bt
fsp
fsp
0.1 mm

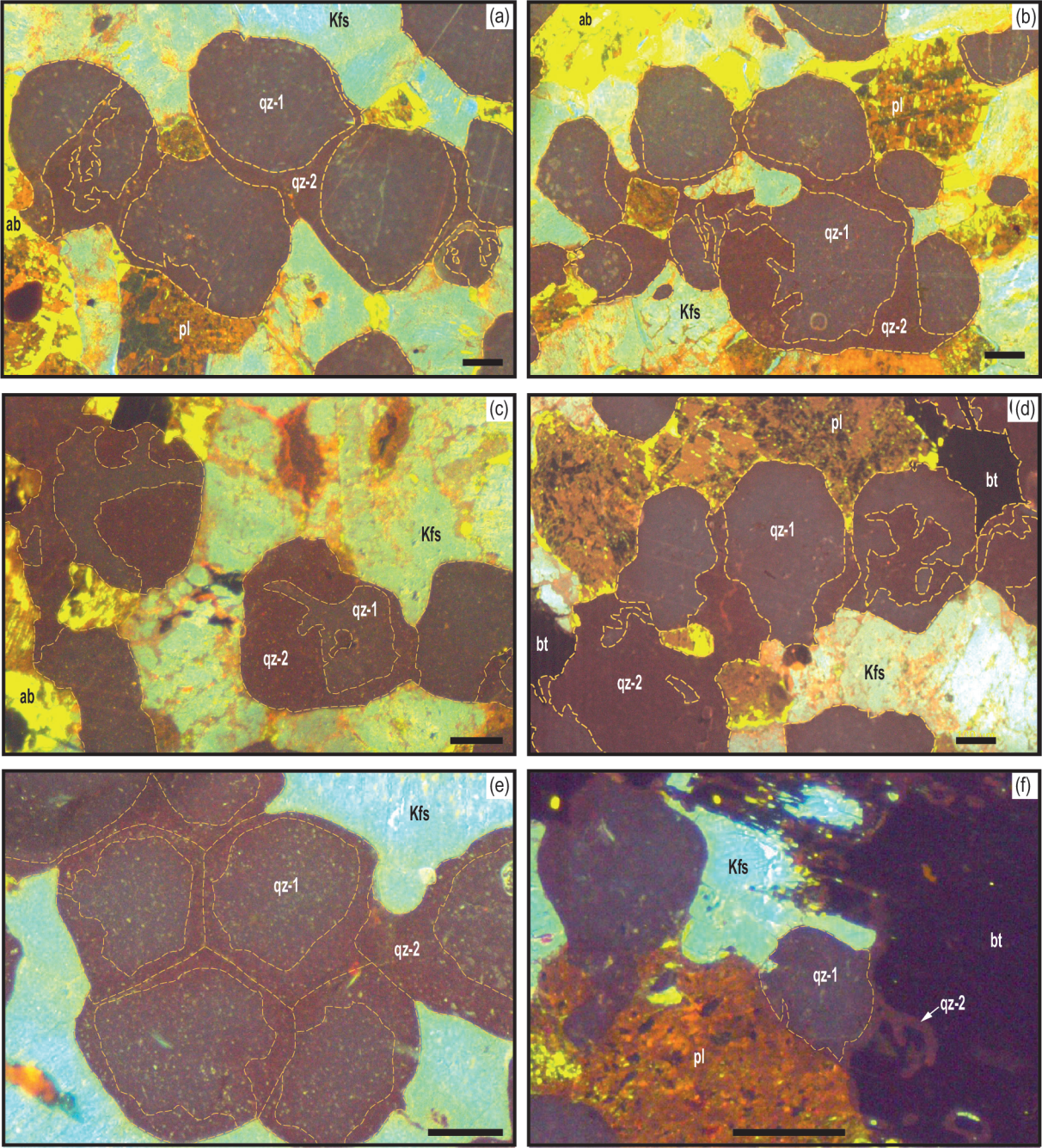
(a)
Kfs
qz-1
qz-2
ab
pl
(b)
ab
pl
qz-1
Kfs
qz-2
(c)
Kfs
qz-1
qz-2
ab
(d)
pl
bt
qz-1
bt
qz-2
Kfs
(e)
Kfs
qz-1
qz-2
(f)
Kfs
bt
qz-1
qz-2
pl

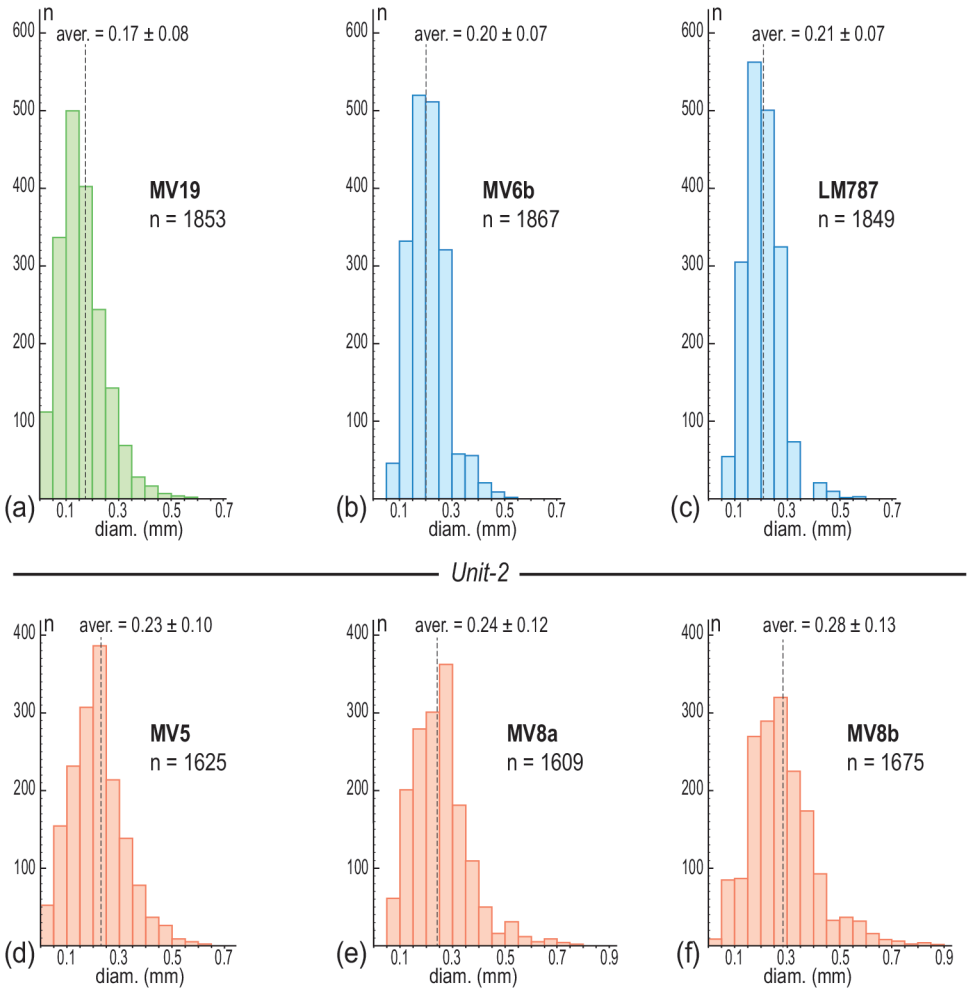
Unit-1
Unit-3
Unit-2
n
aver. = 0.17 ± 0.08
MV19
n = 1853
(a)
aver. = 0.20 ± 0.07
MV6b
n = 1867
(b)
aver. = 0.21 ± 0.07
LM787
n = 1849
(c)
aver. = 0.23 ± 0.10
MV5
n = 1625
(d)
aver. = 0.24 ± 0.12
MV8a
n = 1609
(e)
aver. = 0.28 ± 0.13
MV8b
n = 1675
(f)
diam. (mm)

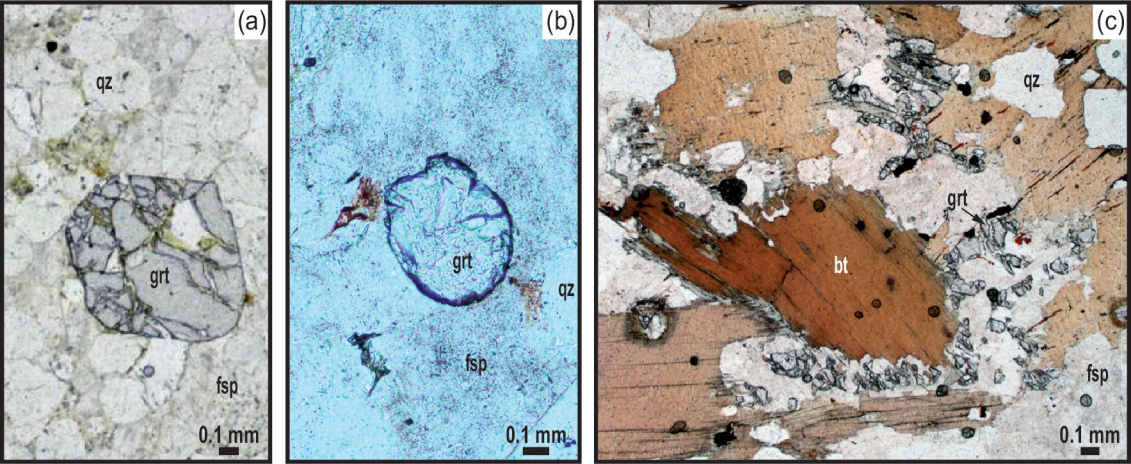
(a)
qz
grt
fsp
0,1 mm
(b)
grt
qz
fsp
0,1 mm
(c)
qz
grt
bt
fsp
0.1 mm

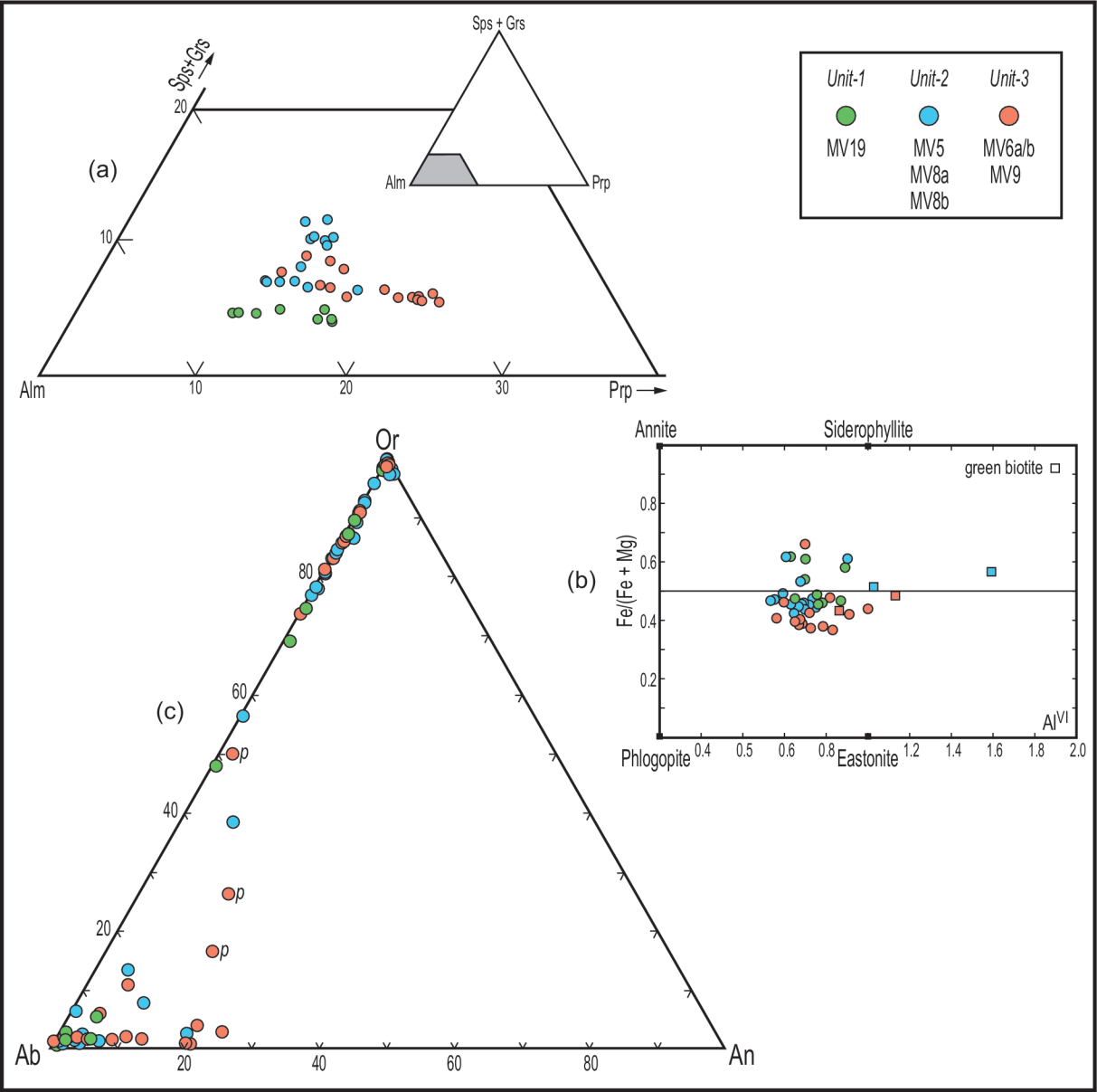
Sps + Grs
Sps+Grs
20
10
(a)
Alm
Prp
Alm
10
20
30
Prp
Unit-1
Unit-2
Unit-3
MV19
MV5
MV8a
MV8b
MV6a/b
MV9
Or
80
60
(c)
40
20
p
p
p
Ab
20
40
60
80
An
Annite
Siderophyllite
green biotite
(b)
Fe/(Fe + Mg)
0.8
0.6
0.4
0.2
AlVI
Phlogopite
0.4
0.5
0.6
0.8
Eastonite
1.2
1.4
1.6
1.8
2.0

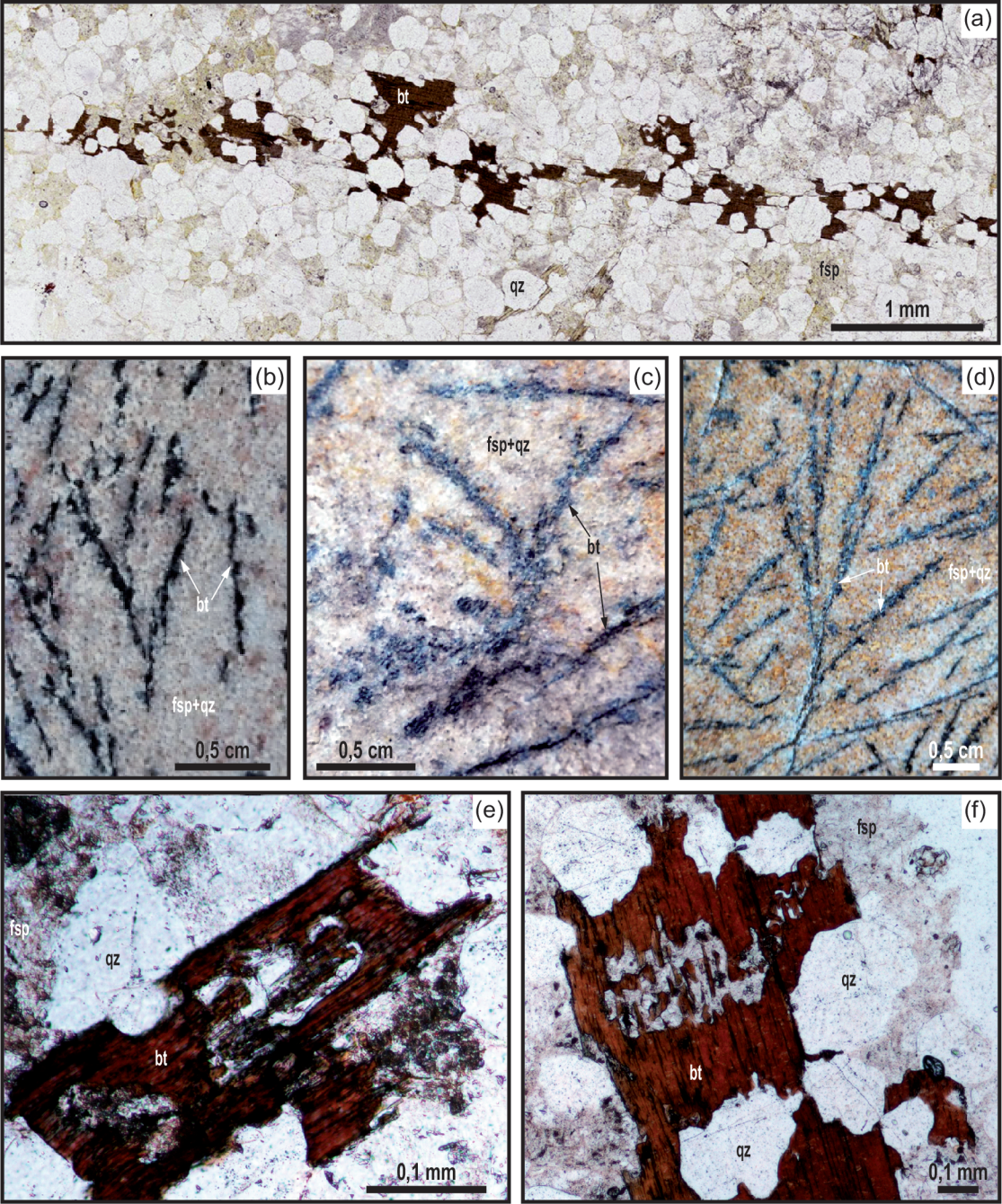
(a)
bt
qz
fsp
1 mm
(b)
bt
fsp+qz
0,5 cm
(c)
fsp+qz
bt
0,5 cm
(d)
bt
fsp+qz
0,5 cm
(e)
fsp
qz
bt
0,1 mm
(f)
fsp
qz
bt
qz
0,1 mm

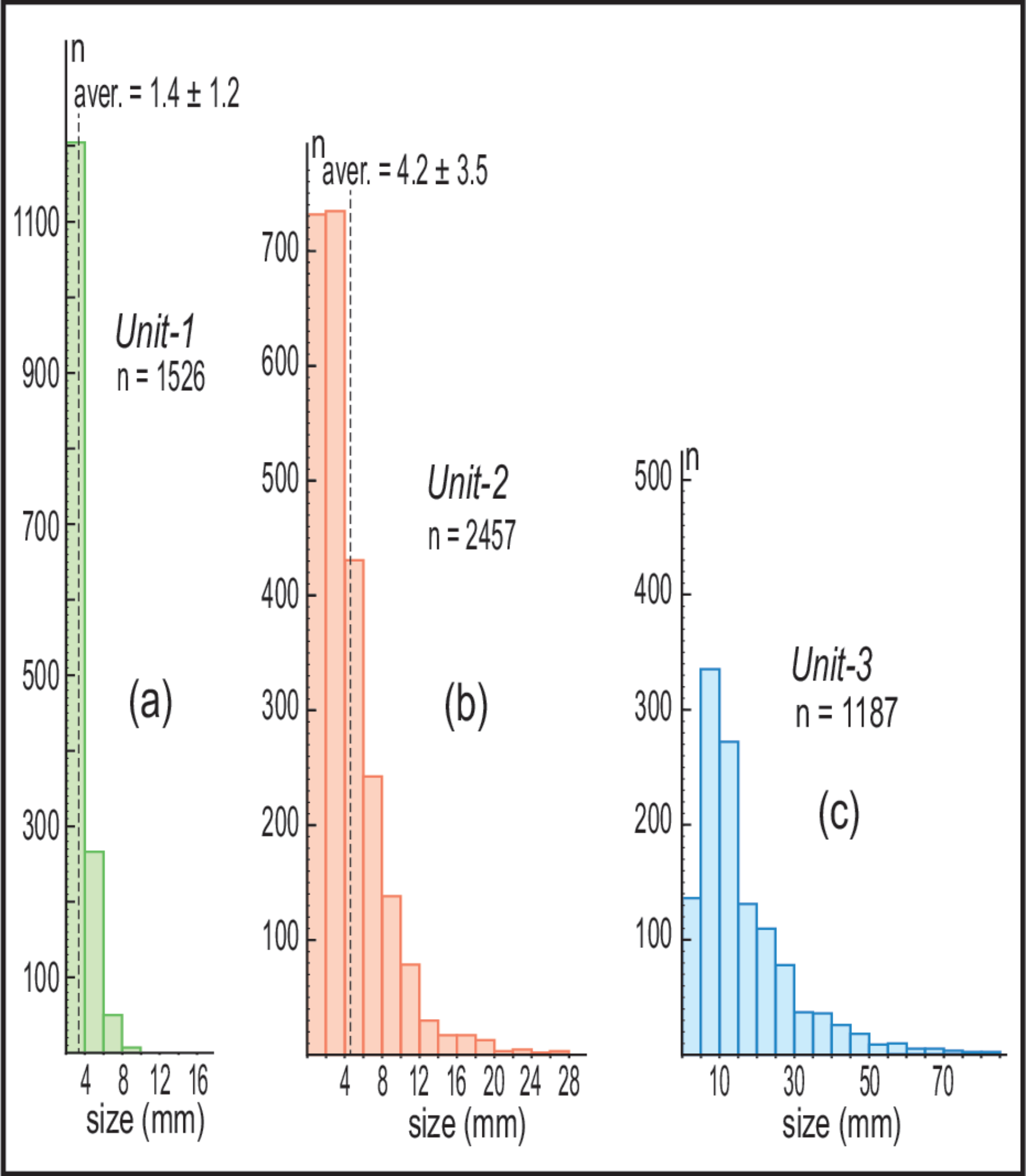
n
aver. = 1.4 ± 1.2
1100
900
700
500
300
100
Unit-1
n = 1526
(a)
4 8 12 16
size (mm)
n
aver. = 4.2 ± 3.5
700
600
500
400
300
200
100
Unit-2
n = 2457
(b)
4 8 12 16 20 24 28
size (mm)
n
500
400
300
200
100
Unit-3
n = 1187
(c)
10 30 50 70
size (mm)

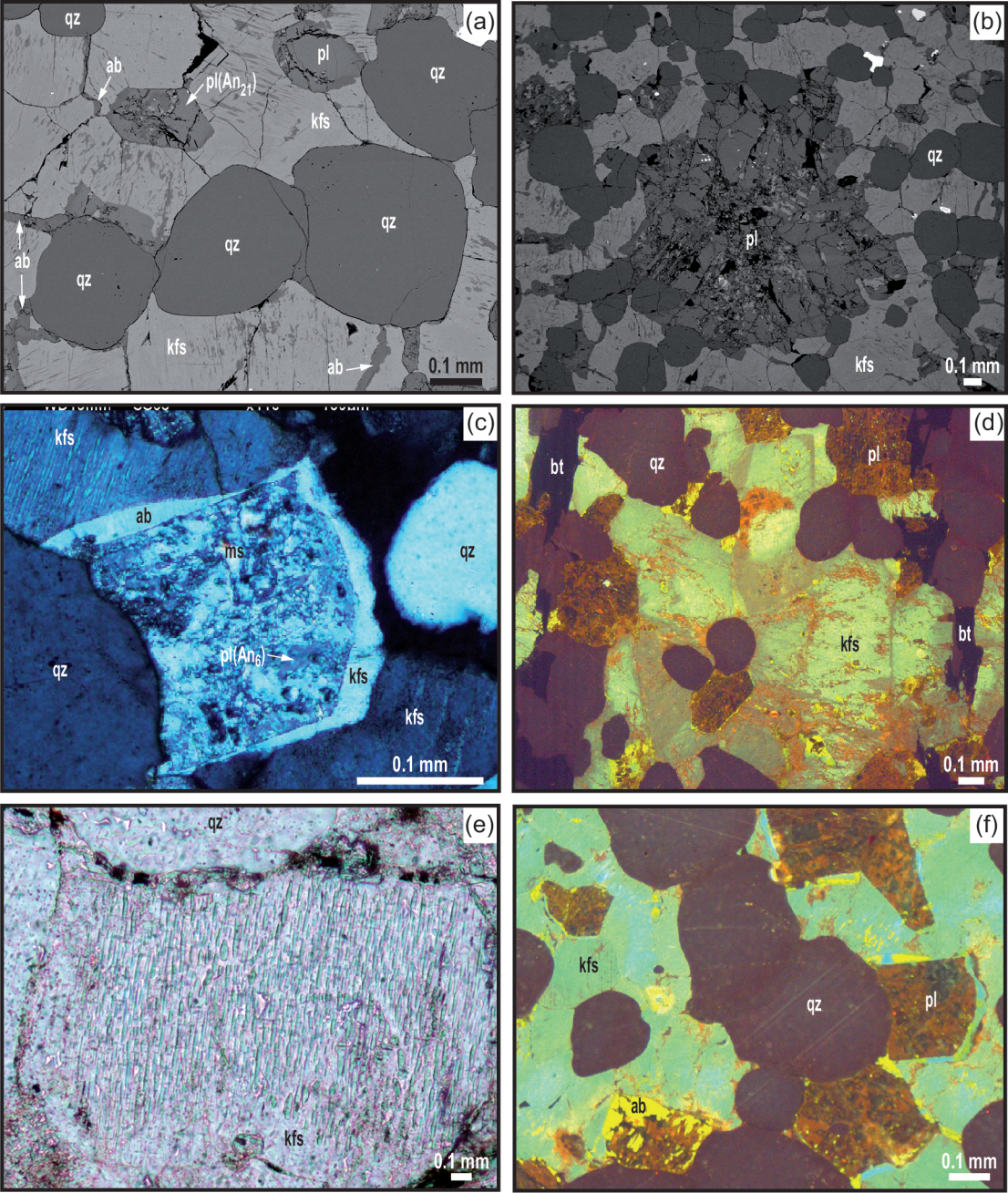
(a)
qz
ab
pl(An21)
pl
qz
kfs
qz
qz
ab
qz
kfs
ab
0.1 mm
(b)
qz
pl
kfs
0.1 mm
(c)
kfs
ab
ms
qz
pl(An6)
qz
kfs
kfs
0.1 mm
(d)
bt
qz
pl
kfs
bt
0.1 mm
(e)
qz
kfs
0.1 mm
(f)
kfs
qz
pl
ab
0.1 mm

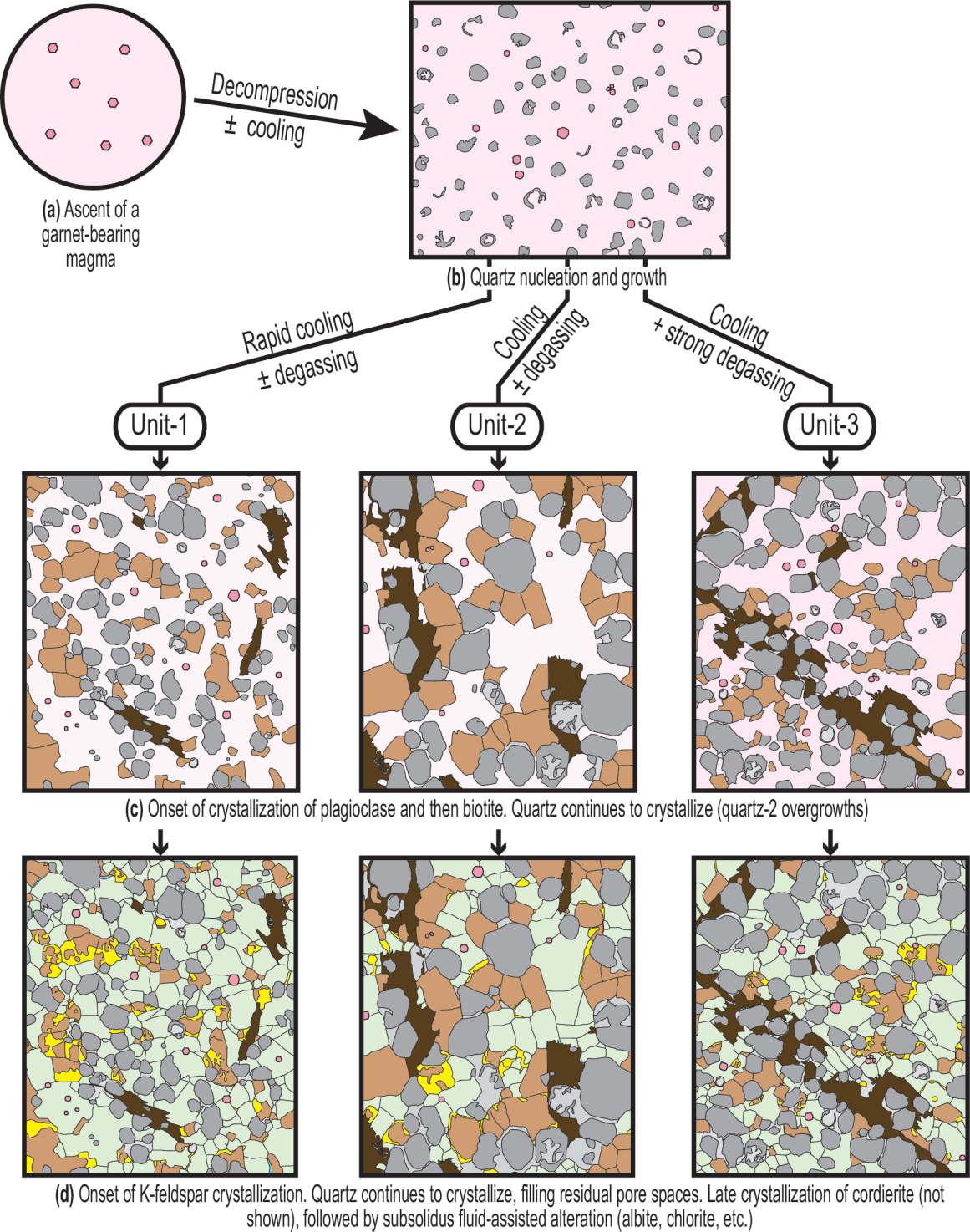
Decompression
± cooling
(a) Ascent of a garnet-bearing magma
(b) Quartz nucleation and growth
Rapid cooling
± degassing
Cooling
± degassing
Cooling
+ strong degassing
Unit-1
Unit-2
Unit-3
(c) Onset of crystallization of plagioclase and then biotite. Quartz continues to crystallize (quartz-2 overgrowths)
(d) Onset of K-feldspar crystallization. Quartz continues to crystallize, filling residual pore spaces. Late crystallization of cordierite (not shown), followed by subsolidus fluid-assisted alteration (albite, chlorite, etc.)

Table 1: Whole-rock major (wt.%) and trace element (µg/g) composition of the three units of the alkali-feldspar granite. Shown for comparison: whole-rock major element composition of Himalayan leucogranite (HL; Scaillet et al., 1995) and Rubicon ignimbrite (RI; Clemens et al., 2012).

Unit	Unit-1		Unit-2		Unit-3		HL	RI
Sample	MV19	MV28	MV8	MV16	MV9	MV20	DK89	9397
SiO_2	74.18	74.03	69.70	74.10	72.86	75.22	73.04	75.77
Al_2O_3	14.19	12.70	14.09	13.01	13.70	13.04	15.32	13.54
FeO^{tot}	1.10	1.89	3.53	1.87	2.41	1.56	0.74	1.69
MnO	–	0.03	0.06	0.03	0.04	0.02	0.01	0.01
MgO	0.32	0.52	1.30	0.60	0.94	0.57	0.20	0.31
CaO	0.24	0.21	0.36	0.30	0.36	0.29	0.85	0.65
Na_2O	2.24	1.88	2.02	2.23	2.61	2.59	3.85	2.64
K_2O	7.08	5.97	6.02	6.27	5.31	5.40	4.96	5.27
TiO_2	0.13	0.23	0.44	0.24	0.29	0.23	0.13	0.11
P_2O_5	0.15	0.12	0.14	0.14	–	0.15	0.14	
LOI	1.29	1.23	1.32	1.04	1.48	1.34	0.79	
Total	100.93	98.80	98.97	99.82	100.00	100.40	100.03	100.00
As	3.7	3.1	4.0	3.0	9.4	7.2		
Ba	429	255	689	333	331	448		
Be	0.7	0.9	1.0	0.9	1.0	1.2		
Co	1.6	2.2	7.2	3.0	4.7	3.1		
Cr	4.8	12	40	13	25	18		
Cs	8.8	7.2	12.7	9.4	11.9	9.4		
Cu	4.3	2.7	11.5	7.1	7.4	6.7		
Ga	17	16	18	16	17	16		
Ge	1.2	1.2	1.5	1.2	1.4	1.4		
Hf	2.3	3.1	4.1	2.8	2.5	2.1		
Nb	2.7	5.8	12	5.1	7.4	6.0		
Ni	43	4.6	80	6.9	60	33		
Pb	11	11	17	23	14	14		
Rb	264	234	236	205	222	211		
Sc	2.3	0.1	12	0.1	7.2	4.9		
Sn	2.4	1.8	3.6	2.7	6.3	5.6		
Sr	51	38	91	56	61	64		
Ta	0.1	0.3	0.9	0.4	1.1	0.7		
Th	1.6	6.9	8.5	5.1	3.7	6.7		
U	0.4	0.6	2.4	1.1	1.5	2.7		
V	4.8	13	49	16	29	21		
W	–	–	1.1	–	1.5	1.5		
Y	33	39	44	32	36	39		
Zn	16	25	55	27	33	28		
Zr	75	106	149	96	93	72		
La	14.02	16.74	27.55	16.57	20.65	21.50		
Ce	28.36	34.07	50.95	32.16	35.57	40.86		
Pr	3.06	3.65	5.66	3.53	3.58	4.38		
Nd	10.34	12.83	20.10	12.36	12.12	15.05		
Sm	2.36	3.57	4.59	2.65	2.51	3.57		
Eu	0.59	0.38	0.99	0.53	0.54	0.61		
Gd	2.60	3.61	4.77	2.83	2.87	3.89		
Tb	0.62	0.79	0.94	0.62	0.65	0.81		
Dy	5.01	6.09	6.80	4.78	5.10	5.92		
Ho	1.16	1.41	1.59	1.16	1.24	1.42		
Er	3.35	3.97	4.66	3.47	3.66	4.25		
Tm	0.53	0.60	0.71	0.56	0.56	0.67		
Yb	3.53	3.66	4.86	3.48	3.70	4.67		
Lu	0.49	0.50	0.69	0.50	0.52	0.67		

FeO^{tot} = total iron as Fe^{2+}; LOI = loss on ignition; – = below detection limit.

Table 2: Whole-rock Sr and Nd isotopic composition of the “spinifex” unit (sample MV9).

Rb (ppm)	222.02	Sm (ppm)	2.51
Sr (ppm)	61.08	Nd (ppm)	12.12
^{87}Rb (µmol)	0.72305	$^{147}Sm/^{144}Nd$	0.1253
^{86}Sr (µmol)	0.06842	$^{143}Nd/^{144}Nd$	0.512066
$^{87}Rb/^{86}Sr$	10.5681	2σ	0.000008
$^{87}Sr/^{86}Sr$	0.776134	$(^{143}Nd/^{144}Nd)_t$	0.511797
2σ	0.000014	$\varepsilon Nd_{(t)}$	-8.2
$(^{87}Sr/^{86}Sr)_t$	0.7265	T_{DM} (Ma)	1865

CHUR composition used to calculate ε_{Nd} values is $^{143}Nd/^{144}Nd = 0.512638$ and $^{147}Sm/^{144}Nd = 0.1967$; the decay constant is $6.54x10^{-12}$; Nd model ages are calculated using $^{143}Nd/^{144}Nd = 0.511580$ for the depleted mantle; $(^{87}Sr/^{86}Sr)_t$, $(^{143}Nd/^{144}Nd)_t$ and $\varepsilon Nd_{(t)}$ calculated at 330 Ma.